UNIVERSIDAD DE SANTIAGO DE CHILE

FACULTAD DE CIENCIA

Departamento de Física

"Macroscopic cavity QED approach using Finite difference Time Domain method"

Jonathan Antonio Sepúlveda Henríquez.

Tesis para optar al grado de Magister en Ciencia con Mención en Física.

Profesor Guía:

Felipe Herrera Urbina.

Santiago – Chile

2019

Jonathan Antonio Sepúlveda Henríquez, 2020

Reconocimiento-NoComercial 4.0 Internacional

Resumen

Recientes experimentos han demostrado la interacción luz-materia en el régimen del acoplamiento fuerte con un emisor molecular individual dentro de una cavidad óptica plasmónica a nanoescala. Para entender completamente la dinámica cuántica de un átomo de dos niveles en tales nanoestructuras dispersivas y absorbentes desde primeros principios, el campo plasmónico debe ser tratado usando un enfoque de electrodinámica cuántica macroscópica. Estudiamos la interacción luz-materia de una molécula orgánica en nanocavidades planas de plata y del tipo Nanoparticle-on-mirror (NPoM, por sus siglas en inglés) construyendo el Hamiltoniano de Jaynes-Cummings en el dominio de frecuencias y resolviendo las ecuaciones de evolución asociadas con kernels no Markovianos. Para una nanoestructura de geometría y composición dada, construimos operadores de campo eléctrico desde el tensor de Green clásico de la cavidad vacía, usando un código propio de Diferencias Finitas en el Dominio del Tiempo (FDTD). Aplicaciones en espectroscopia molecular y química también son discutidos.
Palabras claves: Nanocavidades, tensor de Green, kernel no Markoviano.

Abstract

Recent experiments have demonstrated light-matter interaction in the strong coupling regime with a single organic molecular emitter inside a nanoscale plasmonic optical cavity. In order to fully understand the quantum dynamics of a two-level atom in such dispersive and absorptive optical nanostructures from first principles, the plasmonic field should be treated using macroscopic quantum electrodynamics approach. We study the light-matter interaction of an organic molecule in silver planar and NPoM (Nanoparticle-on-mirror) nanocavities by constructing the Jaynes-Cummings Hamiltonian in the frequency-domain and solving the associated evolution equations with non-Markovian kernels. For a given nanostructure geometry and material composition, we construct electric field operators from the classical Green tensor of the empty cavity problem, using home-built code for the Finite Difference Time Domain (FDTD) method. Applications in single-molecule spectroscopy and chemistry are also discussed.

Key words: Nanocavities, Green's tensor, non-Markovian kernel.

Acknowledgment

This research has been supported by Fondecyt Regular Grant No. 1181743 and Iniciativa Científica Milenio (ICM) through the Millennium Institute for Research in Optics (MIRO).

Contents

List of Tables

List of Figures

Introduction

In the last two decades, Surface Plasmon Polaritons (SPPs) in metal dielectric interfaces have been intensely studied in the field of Nanophotonics, which is broadly defined as the study of electromagnetic fields that are confined below the diffraction limit [Maier, 2007].
Metals are characterized by a negative real permittivity [Maier, 2007] in the near infrared up to optical frequencies. Light is able to penetrate by only a small amount into the metal bulk. Which makes it possible that in a metal-dielectric interface the electromagnetic field becomes very localized in regions of the space on the order of tens nanometers [Carnegie et al., 2018, Kongsuwan et al., 2017]. These confined modes are known as Surface Plasmons, described primarily by a considerable enhancement of the electromagnetic field relative to free space with evanescent decay from the surface of the metal [Maier, 2007]. Therefore, light-matter interaction in these systems is not only influenced by the confinement and the manipulation of electromagnetic radiation due to geometrical effects as in waveguides and resonant cavities, but also by the optical response of the materials involved.
Nanophotonic devices that operate in the range of frequencies mentioned above, have several applications in Surface-Enhanced Raman Scattering SERS [Nguyen et al., 2015], improved efficiency of solar cells [Atwater H. A., 2010], cancer treatment [Lal et al., 2008], biological sensing [Huang et al., 2009], among other applications. These topics have been described in the literature using classical electrodynamics, mainly due to the large number of excitations contained in the electromagnetic fields of the lasers used [Maier, 2007]. However, the extreme localization of plasmonic fields have brought the idea of the miniaturization of photonic devices based on plasmonic waveguides [Maradudin A., 2014], stimulating the interest on studying the quantum properties of surface plasmons, in particular, in a regime of a few plasmons, where the generation and detection of single surface plasmons and the strong interaction between the plasmonic field with dipolar emitters, can enable quantum coherence in the light-matter interaction process.
To understand light-matter interaction from first principles, we need quantum electrodynamics (QED) [Buhmann, 2012]. However, the systems with structures in nanoscales are often too complex to solve analytically with QED in an exact way [Novotny L., 2009]. An important example of this type of problems are nanocavities of the nanoparticle-on-mirror NPoM type, whose nanogaps are used to probe properties of single molecules via Raman scattering, nonlinear effects, chirality or spontaneous emission [Chikkaraddy et al., 2017]. The production of confined fields on atomic scales are essential for the observation and control of chemical reactions at the level of individual molecules [Ueno K., 2013, Herrera F., 2017]. The experimental use of gold nanocubes or other nonspherical geometries makes an analytical analysis unfeasible due to the lack of symmetry. We thus need to use numerical methods to solve this kind of systems and contrast theoretical

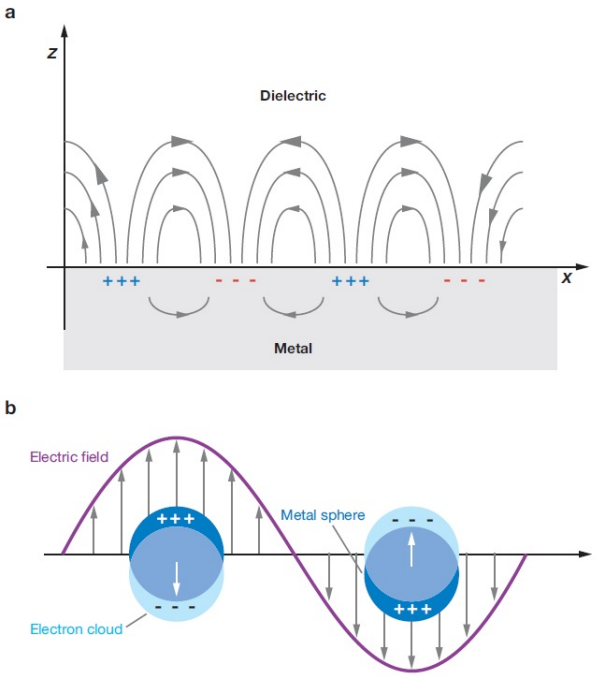

Figure 0.0.1: Schematic Surface Plasmon Polaritons diagrams ilustrating (a) Propagating surface plasmon modes in the interface metal-dielectric and (b) Localized surface plasmon modes in a metal nanoparticle. Adapted from Ref.[Willets K. A., 2007].

predictions with experimental results.

One numerical tool that allows us to solve this kind of problem is the Finite Difference Time Domain method (FDTD) [Taflove A., 2005, Kunz, 1993], introduced by Kane Yee [Yee, 1966]. This method solves Maxwell's equations in time domain by finite difference for three dimensional structures and has been used widely in plasmonics over the past decade [Wang et al., 2019, Taflove A., 2013].

Chapter 1

Motivation

1.1 Surface Plasmon Polaritons

Efficient coupling between a single emitter with the near field of a plasmonic nanostructure, is an important goal of quantum plasmonic [Maradudin A., 2014]. Developing new techniques to control and manipulate the interaction between light and matter at the nanoscale is an important goal in science and engineering.

The extreme confinement of light in plasmonic environments made of noble metal nanostructures is due to surface modes, called Surface Plasmon Polaritons (SPPs) [Willets K. A., 2007], that are electromagnetic excitations propagating at the interface between a dielectric and a conductor, evanescently in the perpendicular direction (propagating surface plasmon), or confined modes in metal nanoparticles, where light interacts with particles much smaller than the incident wavelength (localized surface plasmon), these two types of plasmon excitations are illustrated in Figure (0.0.1). These plasmonic modes arise via the coupling of electromagnetic fields with the free conduction electrons in the metal near the vicinity of a dielectric-metal interface.

The electromagnetic fields of plasmonic excitations are localized to within a wavelength from the interface, with the result that their excitation produces a significant enhancement of the electromagnetic field in the immediate vicinity of the interface, relative to the free space.

In the optical regime, the dielectric properties of metals can be explained by a plasma model, where the free electrons move in a background of fixed positive ions (phonons are ignored) under the influence of an external electromagnetic excitation. The optical response of this electron plasma governs all optical properties of metals, at least in the visible part of the spectrum, where its resonant energies reside. The electric response of metals may be addressed by using the Drude model [Ru E. C., 2009]. One can write a simple equation of motion for an electron in the plasma subject to an external electric field [Maier, 2007]

$$m\ddot{\mathbf{x}} + m\gamma_p\dot{\mathbf{x}} = -e\mathbf{E} \tag{1.1.1}$$

where m and e are the effective mass and the free electron charge, γ_p is the characteristic collision frequency and $\mathbf{E}$ is the electric field. If we assume a harmonic time dependence $\mathbf{E}(t) = \mathbf{E}_0 e^{-i\omega t}$, making the ansatz $\mathbf{x}(t) = \mathbf{x}_0 e^{-i\omega t}$ and substituting in equation (1.1.1), it can be shown that the

permittivity can be given in the form [Maier, 2007]

$$\epsilon_r(\omega) = \epsilon_\infty - \frac{\omega_p^2}{\omega^2 + i\gamma_p\omega} \tag{1.1.2}$$

where $\omega_p = \sqrt{\frac{Ne^2}{m\epsilon_0}}$ is the plasma frequency of the free electrons and γ_p is the collision frequency, which reflects the damping experienced by the electrons when moving within the material and ϵ_∞ accounts for the residual polarization due to the positive background of ions cores. The positive collision frequency γ_p, present for an absorbing medium ensures that the imaginary part of $\epsilon_r(\omega)$, is positive for all real ω, leading to wave absorption.

For a piecewise dielectric metal medium as in Figure (0.0.1), where ϵ_1 is the permittivity of the dielectric medium and $\epsilon_2(\omega)$ correspond to the metal medium, the frequency of SPPs are related to the plasma frequency as [Maier, 2007]

$$\omega_{sp} = \frac{\omega_p}{\sqrt{\epsilon_1 + \epsilon_2(\omega)}} \tag{1.1.3}$$

the plasmon resonant condition, thus occurs when

$$\epsilon_1 + \epsilon_2(\omega) = 0. \tag{1.1.4}$$

Surface Plasmons Polaritons on closely spaced multiple nanostructures can hybridize with each other to create trapped modes within their gap. Such nanogaps are used to probe optical properties of single molecules such as their Raman scattering [Ru E. C., 2012], nonlinear effects [Kauranen M., 2012], chiral activity [Valev et al., 2013] or rate of emission [Giannini et al., 2011]. The systematic analysis of the Purcell factors shows that modes with optical field perpendicular to the gap are best to probe the optical properties of cavity-bound emitters, such as single molecules [Chikkaraddy et al., 2017].

As equation (1.1.2) shows, the permittivity of a linear dielectric is a complex function of frequency. The real and imaginary parts describing the effects of dispersion and absorption respectively and are related by the Kramers-Kroning relations

$$\mathrm{Re}\left[\epsilon_r(\omega)\right] - 1 = \frac{P}{\pi}\int_{-\infty}^{\infty} d\omega' \frac{\mathrm{Im}\left[\epsilon_r(\omega')\right]}{\omega' - \omega} \tag{1.1.5a}$$

$$\mathrm{Im}\left[\epsilon_r(\omega)\right] = -\frac{P}{\pi}\int_{-\infty}^{\infty} d\omega' \frac{\mathrm{Re}\left[\epsilon_r(\omega') - 1\right]}{\omega' - \omega} \tag{1.1.5b}$$

where P denotes the principal value.

Since dispersion is always associated with absorption, the losses must necessarily be included into a rigorous quantization scheme. Using a Hopfield model of a linear homogeneous lossy dispersive dielectric [Hopfield, 1958] and representing the medium by a collection of interacting bosonic matter fields, Huttner and Barnett [Huttner B., 1992] presented a canonical quantization scheme for an electromagnetic field in the dielectric, both dispersion and absorption are taken into account in a quantum mechanically consistent way. This approach was later extended by Knoll [Knoll et al., 2000], to arrive at a consistent theory of field quantization in media known as macroscopic QED [Scheel S., 2008].

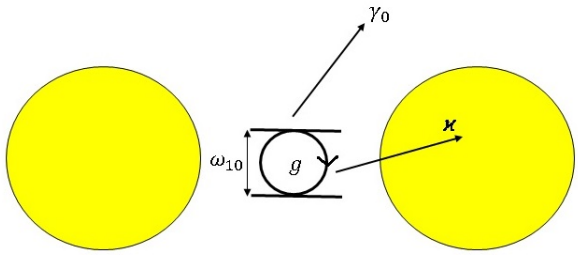

Figure 1.1.1: Schematic illustration of a plasmonic nanocavity system. A two level atom with resonant frequency ω_{10} is located between two gold metals nanoparticles, with the atom-cavity coupling given by g. There are two channels by which light can leak out from this configuration, directly through the nanoparticles with rate κ or via off-axis radiation to the far field with rate γ_0.

1.2 Single Emitter cavity interaction

The electronic states of a single atom or molecule, considered in isolation, are stationary solutions of the Schrödinger equation. There is no apparent reason for an electron to decay, except for external perturbations in the local photonic environment acting on this quantum system. There is a variety of quantum systems such as atoms, molecules, semiconductor quantum dots, NV centers in diamonds and superconducting quantum bits that can be used as single emitters [Karanikolas, 2016], with applications ranging from light-emitting diodes to fluorescent dyes, colorants, clinical assays, etc [Giannini et al., 2011].

The ability of a single emitter to produce a photon, therefore, depends not only on the intrinsic properties of the emitter, but also on the local photonic environment. Thus, changing the photonic environment can be used to modify the emission rate, with potential applications in sensing, integrated photonic and solar energy conversion [Pelton, 2015].

One of the most successful methods of manipulating quantum ligth-matter interaction, has been through the use of cavities. Plasmonic modes can be squeezed into volumes far below the diffraction limit and therefore provide an excellent interface between single photons and emitters. This extreme manipulation changes the photonic environment, alters the lifetime of the excited state by making it easier or harder for the emitter to relax via emitting a photon [Hugall et al., 2018]. The use of a cavity acts to increase the local density of states (LDOS) that is the number of electromagnetic modes, per unit frequency and per unit volume, available for the emitter to radiate by increasing the interaction strength between the emitters and the cavity [Narayanaswamy A., 2010]. Enhancing the LDOS through the use of small cavities has shown to be a very effective method for increasing the radiative decay rate of an emitter via the Purcell effect [Purcell, 1995]. An emitter experiences the increase of LDOS and emits photons more efficiently.

In the electric dipole approximation, the interaction strength between the cavity and the emitter is defined by the atom field coupling strength [Hugall et al., 2018]

$$g = \mathbf{d} \cdot \mathbf{E}(\mathbf{r}, \omega) \tag{1.2.1}$$

where $\mathbf{d}$ is the emitter's transition dipole moment, $\mathbf{r}$ is the displacement between the emitter and

the cavity and ω is the resonant frequency of the emitter and the cavity.

The effective strength of g is measured relative to the losses or decay rates in the system, typically from photons leaking through the cavity mirrors with rate κ or escaping directly from cavity to the far field with rate γ_0 as the Figure (1.1.1) shows. The comparison of these rates with g, define the so-called weak and strong coupling regimes.

For the case of $g \ll (\kappa, \gamma_0)$, the system is said to be in the weak coupling regime, the coupling strength is such that energy exchange from the emitter to the cavity occurs but is nonreversible and incoherent, characterized by monotonous exponential decay of atomic excitation. This decay rate can be increased or decreased compared to the free space emission value, depending on whether the atomic transition frequency is adjusted to the cavity resonance or not. In this regime, the emitter and the cavity remain separate quantum entities, in other words, the enhancement occurs without changing the photon energy and the energy levels of the emitter remain unchanged. The cavity losses prevent coupling back to the emitter and the energy has a one directional flow. In this regime, the light-matter interaction can be treated perturbatively. In the strong coupling regime $g \gg (\kappa, \gamma_0)$, the coupling strength is so large that the emitter and the cavity become a new single quantum object with energy shared coherently and reversibly between them. This regime is characterized by reversible Rabi oscillations of the atomic excitations, where the energy of the initial excited state is periodically exchanged between the cavity and the emitter. Strong coupling between a cavity mode and electronic or vibrational molecular transitions is well know to result in polariton formation [Herrera F., 2016].

Nowadays it is possible to achieve single-emitter strong coupling at room temperature in ambient conditions using nanoparticle-on-mirror (NPoM) geometries [Chikkaraddy et al., 2016], i.e, placing the emitter in the gap between nanoparticles and a metal film. This gap is accurately controlled using molecular spacers, where only one molecular emitter can fit in the nanogap with its transition dipole moment perfectly aligned. Figure (1.2.1) shows the quality factor Q for each type of nanocavities, whispering gallery spheres, microdisks, photonic crystals, micropillars and

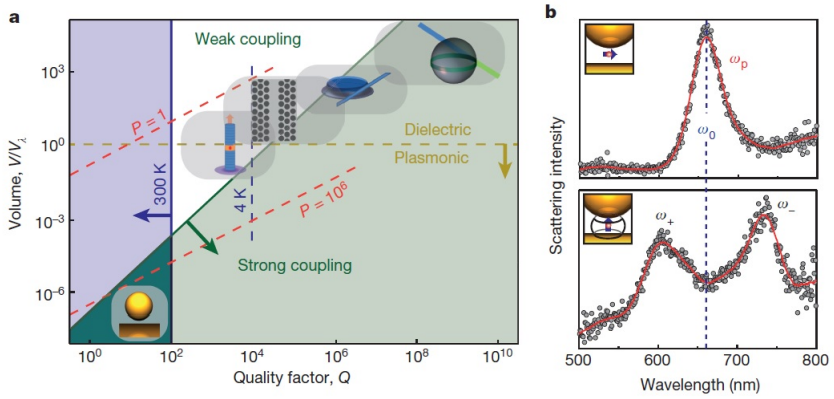

Figure 1.2.1: Single-emitter optical cavities. (a) The quality factor of an optical cavity Q is plotted against its effective volume, with $V_\lambda = (\lambda/n)^3$. We can see that NPoM is at the room temperature region with strong coupling (green arrow) and a Purcell factor $P = 10^6$. (b) Scattering spectra of isolated NPoM, for two different transition dipolar moment $\mathbf{d}_A$ configurations (methylene-blue dye). With a dipole moment parallel to the mirror, only a plasmon peak ω_p appears, and this is identical to the NPoM without emitter. With a dipole moment perpendicular to the mirror, split peaks appear which is the result of the strong coupling interaction between the emitter and the plasmon. Taken from Ref.[Chikkaraddy et al., 2016].

nanoparticle-on-mirror used to date in experiments [Chikkaraddy et al., 2016]. The NPoM is at the region of strong coupling and room temperature. The dark-field scattering spectra shows different orientations of the emitter. With a transition dipole moment parallel to the mirror, the resonant scattering plasmonic peak ω_p is identical to the NPoM without any emitter however, with a transition dipole moment perpendicular to the mirror, the spectra shows two split peaks ω_+ and ω_- resulting from the light-molecule strong coupling interaction.

1.3 Strong coupling for controlled chemical reactions

Strongly coupled systems are useful for many applications in light-matter interactions for example to control chemical reactions [Hutchison et al., 2012], where the interaction can overcome decoherence effects. Using an optical cavity tuned to a transition to an excited state, even in the absence of photons, a splitting always exists due to coupling vacuum fields in the cavity. In this context, the molecules and the cavity form a single entity with new energy levels, as illustrating in Figure (1.3.1). These hybrid states are called polaritons, and have been shown to have its own distinct chemistry [Herrera F., 2020].

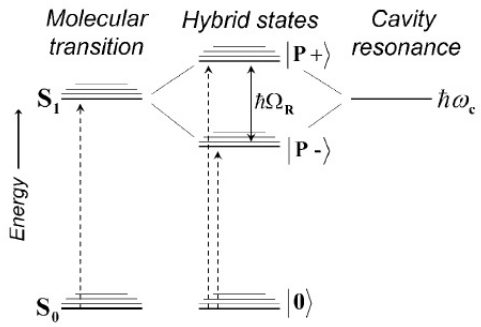

Figure 1.3.1: Showing the energy levels of the interaction of a HOMO-LUMO $(S_0 - S_1)$ transition of a molecule resonant with a cavity mode $\hbar\omega_c$. Strong coupling regime leads to formation of two hybrid light-matter states $|P+\rangle$ and $|P-\rangle$, separated by the Rabi splitting energy $\hbar\Omega_R$. Taken from Ref.[Hutchison et al., 2012].

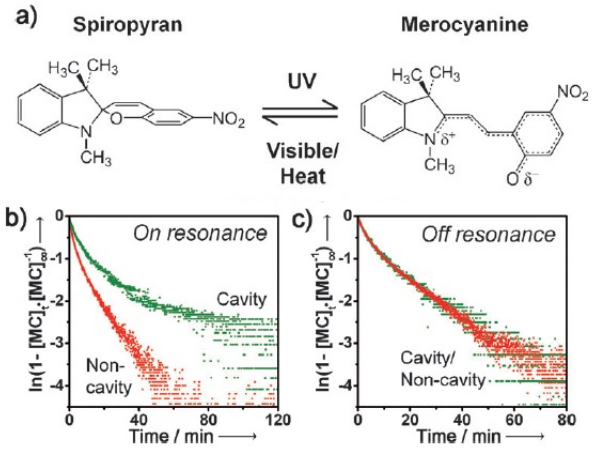

Figure 1.3.2: (a) Molecular structure of spiropyran (SPI) and merocyanine (MC). (b) Kinetics of the growth of the MC absorbance (concentration) measured for the bare molecules (red) and the coupled system (green). (c) The cavity is in off resonance with the MC absorption, the photoisomerization rate is identical to that of the non-cavity sample. Taken from Ref.[Hutchison et al., 2012].

To demonstrate the modified chemistry of molecular polaritons, in Ref.[Hutchison et al., 2012], the group of Ebbesen chose a photochromic molecule spiropyran (SPI), which undergoes isomerization following photoexcitation to form a merocyanine (MC), this chemical reaction is unimolecular to avoid any complications due to diffusion. Using a two silver mirrors cavity, insulated with a thin poly (vinyl alcohol) (PVA) films.

Analyzing the photoisomerization kinetics Figure (1.3.2) inside and outside the cavity, they saw that the photoisomerization rate is slowed down significantly in the cavity structure. This retardation corresponds to the onset of strong coupling regime and the formation of the new hybrid light-matter states.

1.4 Numerical study of single emitters under strong coupling in cavities

In order to physically model and describe electromagnetic systems composed of gold and silver in quantum optics, some of the most powerful approaches usually require the classical Green's tensor of the system $\overleftrightarrow{\mathbf{G}}(\mathbf{r},\mathbf{r}';\omega)$. The Green's tensor is the solution of Maxwell's equation at location $\mathbf{r}$, with frequency ω given a dipole source located at $\mathbf{r}'$ together with boundary conditions, and represents the electric field radiated at position $\mathbf{r}$ by three orthogonal dipoles located at $\mathbf{r}'$. The LDOS is related to the imaginary part of the Green's tensor by [Novotny L., 2009]

$$\mathrm{LDOS}_l(\mathbf{r},\omega) = \frac{6\omega}{\pi c^2}\mathrm{Im}\left[\mathbf{n}_l \cdot \overleftrightarrow{\mathbf{G}}(\mathbf{r},\mathbf{r}';\omega)\cdot \mathbf{n}_l\right] \tag{1.4.1}$$

where $l = x, y, z$ directions. The dipole decay rate is proportional to the LDOS, which depends on the transition dipole defined by the two level atom involved in the transition, as given by [Novotny L., 2009]

$$\gamma_0 = \frac{\pi\omega}{3\hbar\epsilon_0}\mathrm{LDOS}_l(\mathbf{r},\omega). \tag{1.4.2}$$

This relation allows us to calculate the spontaneous decay rate of a two-level atom in an arbitrary reference system. All that is needed is the knowledge of the Green's tensor for the system.

In free space, the LDOS has its usual form [Joulain et al., 2003]

$$\mathrm{LDOS} = \frac{\omega^2}{\pi^2 c^3} \tag{1.4.3}$$

so the atomic decay rate is given by

$$\gamma_0 = \frac{\omega^3 \left|\mathbf{d}_A^{mn}\right|^2}{3\pi\epsilon_0\hbar c^3} \tag{1.4.4}$$

where $\mathbf{d}_A^{mn} = \langle m_A|\,\hat{\mathbf{d}}_A\,|n_A\rangle$ is the transition dipole matrix element. This expression can also be obtained with the Fermi's Golden rule.

Many techniques in quantum optics require the knowledge of the Green's tensor of a system, but the Green's tensor is only known analytically for very simple geometries, for example, planar multilayer systems [Paulus et al., 2000]. In this case, the Green's tensor must take into account all the reflections and refractions that occur at different interfaces. The Green's tensor for this giving geometry has two contributions of the form [Paulus et al., 2000]

$$\overleftrightarrow{\mathbf{G}}(\mathbf{r},\mathbf{r}';\omega) = \overleftrightarrow{\mathbf{G}}^0(\mathbf{r},\mathbf{r}';\omega) + \overleftrightarrow{\mathbf{G}}^{scatt}(\mathbf{r},\mathbf{r}';\omega) \tag{1.4.5}$$

where $\overleftrightarrow{\mathbf{G}}^0(\mathbf{r},\mathbf{r}';\omega)$ is the homogeneous Green's tensor and $\overleftrightarrow{\mathbf{G}}^{scatt}(\mathbf{r},\mathbf{r}';\omega)$ is the reflection contribution coming from interactions with the materials and is given by

$$\overleftrightarrow{\mathbf{G}}^{scatt}(\mathbf{r},\mathbf{r}';\omega) = \frac{i}{4\pi}\int_0^\infty dk_\rho \frac{k_\rho}{k_z} e^{ik_z R_z}\left(\overleftrightarrow{\boldsymbol{g}}_s - \frac{k_z^2}{k_0^2}\overleftrightarrow{\boldsymbol{g}}_p\right) \tag{1.4.6}$$

where $k_z = \sqrt{k_0^2 - k_\rho^2}$, $k_0 = \omega/c$, $R_z = \mathbf{r} - \mathbf{r}'$ and $k_\rho = \sqrt{k_x^2 + k_y^2}$ is the component to the wavevector parallel to the surface. The two tensors $\overleftrightarrow{\boldsymbol{g}}_s$ and $\overleftrightarrow{\boldsymbol{g}}_p$ are given by [Wu et al., 2018]

$$\overleftrightarrow{\boldsymbol{g}}_s = \frac{r_s e^{2ik_z z'}}{2} \begin{pmatrix} J_0(k_\rho\rho) + J_2(k_\rho\rho)\cos(2\phi) & J_2(k_\rho\rho)\sin(2\phi) & 0 \\ J_2(k_\rho\rho)\sin(2\phi) & J_0(k_\rho\rho) - J_2(k_\rho\rho)\cos(2\phi) & 0 \\ 0 & 0 & 0 \end{pmatrix} \tag{1.4.7a}$$

$$\overleftrightarrow{\boldsymbol{g}}_p = r_p e^{2ik_z z'} \begin{pmatrix} \frac{1}{2}\left[J_0(k_\rho\rho) - J_2(k_\rho\rho)\cos(2\phi)\right] & \frac{1}{2}J_2(k_\rho\rho)\sin(2\phi) & i\frac{k_\rho}{k_z}J_1(k_\rho\rho)\cos(\phi) \\ \frac{1}{2}J_2(k_\rho\rho)\sin(2\phi) & \frac{1}{2}\left[J_0(k_\rho\rho) + J_2(k_\rho\rho)\cos(2\phi)\right] & i\frac{k_\rho}{k_z}J_1(k_\rho\rho)\sin(\phi) \\ -i\frac{k_\rho}{k_z}J_1(k_\rho\rho)\cos(\phi) & -i\frac{k_\rho}{k_z}J_1(k_\rho\rho)\sin(\phi) & -\frac{k_\rho^2}{k_z^2}J_0(k_\rho\rho) \end{pmatrix} \tag{1.4.7b}$$

where $\rho = \sqrt{(x-x')^2 + (y-y')^2}$ is the distance between the source and the observation point and $\phi = \tan^{-1}\left({}^{(y-y')}/_{(x-x')}\right)$. The functions r_s and r_p are the Fresnel coefficients due to the reflection waves in the interface. For local and nonmagnetic materials, these coefficients are

$$r_s = \frac{k_z - k_{2z}}{k_z + k_{2z}} \tag{1.4.8a}$$

$$r_p = \frac{\epsilon(\omega)k_z - k_{2z}}{\epsilon(\omega)k_z + k_{2z}} \tag{1.4.8b}$$

where $k_{2z} = \sqrt{\epsilon(\omega)k_0^2 - k_\rho^2}$. Equation (1.4.6) is called Sommerfeld integral and relates a spherical wave from a point source to a convolution set of plane and cylindrical waves. This equation does not have analytical solutions and must be evaluated numerically, and care must be taken doing so, due to the potential presence of singularities in k_z and the reflections coefficients.

The calculation of the spherical multilayer Green's tensor, follows from the same ideas as the planar multilayer Green's tensor and is given in [Li et al., 2001].

Finding a computational solution to Maxwell's equations to model nanostructures with arbitrarily form, has become popular over time. There are different numerical methods that try to provide solutions to plasmonic problems with arbitrary geometries.

In this thesis, it was chosen to work with the Finite Difference Time Domain method (FDTD), due to its multiple advantages among which the following stand out:

- The FDTD algorithm discretizes Maxwell's equations in space and time, giving second-order precision.
- The solutions generated by this method are in the time domain and as a result the dispersive and non-linear effects can be treated.
- Different types of sources can be included with the option of using electromagnetic pulse propagation to analyze a wide range of frequencies.
- Various types of geometries can be used, from the simplest such as spheres, cubes and cylinders to more complex structures.

There are many software packages that implement the FDTD method, such as Lumerical, Meep, GSVIT or Angora to name a few. However, in this thesis, we use a home-built FDTD code written in MATLAB®, which is a software widely used in science and engineering.

Chapter 2

The Finite Difference Time Domain Method

2.1 General features

In 1966, Kane Yee designed the finite difference time domain (FDTD) method [Yee, 1966]. This algorithm solves Maxwell's equations, specifically the Faraday's and Ampere's laws for both electric and magnetic fields in time and space. This formulation only works with the electromagnetic fields and not with the electric and magnetic fluxes.

The FDTD method has gained big popularity, due to the recent development of more robust computational tools. For example, the method is easy to implement using in parallel architectures, which is a big advantage to model problems in the time domain. Even though, the method solves the electromagnetic fields in the time domain, it is possible obtain information the frequency domain by Fourier transformation [Schneider, 2012].

The FDTD method defines a computational space, in which various structures can be defined. Commonly used geometries include spheres, cubes and cylinders or even more complex structures [Berens et al., 2016], as illustrated in Figure (2.1.1). The structures can be chosen to be dielectric or magnetic materials, perfect conductors [Schneider, 2012], real metals [Teixeira, 2008], nonlinear materials [Dissanayake et al., 2010], anisotropic materials [Dou L., 2006], or materials with an arbitrary dielectric response.

The versatility of the FDTD method allows us to solve a large variety of electromagnetic problems, how to obtain scattering spectra and radar cross sections [Luebbers et al., 1993], model antennas [Makinen et al., 2002], crystalline structures [Yokoyama M., 2005], medical devices [Rahmat-Samii Y., 2006], geological structures [Liu et al., 2007], microwave circuits [Reddy V. S., 1999], optical fibers [Perez-Ocon et al., 2006] and plasmonic devices [Taflove A., 2013, Paul S. R., 2016].

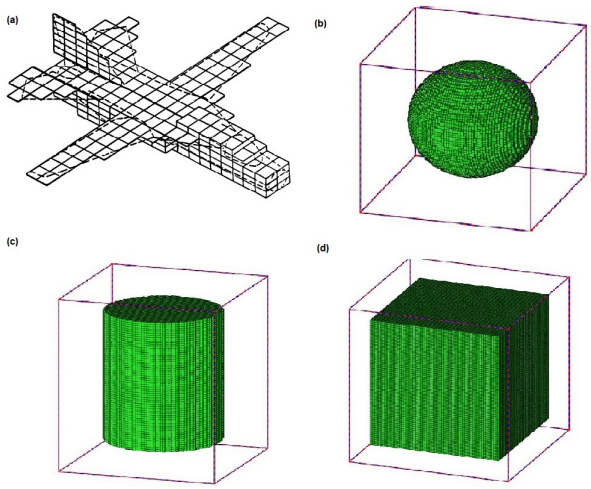

Figure 2.1.1: Geometries that can be implemented using the FDTD algorithm. The plane was taken from Ref.[Kunz, 1993].

2.2 Discretization of Maxwell's equations

Let us consider a box or a region of space without electric or magnetic current sources. In MKS units, the time-domain Maxwell's equation are given in differential form by [Jackson, 1998]

$$\nabla \cdot \mathbf{D} = 0 \tag{2.2.1a}$$

$$\nabla \cdot \mathbf{B} = 0 \tag{2.2.1b}$$

$$\frac{\partial \mathbf{B}}{\partial t} = -\nabla \times \mathbf{E} - \mathbf{M} \tag{2.2.1c}$$

$$\frac{\partial \mathbf{D}}{\partial t} = \nabla \times \mathbf{H} - \mathbf{J} \tag{2.2.1d}$$

where, $\mathbf{D}$ is the electric flux density in $[C/m^2]$, $\mathbf{B}$ is the magnetic flux density in $[Wb/m^2]$. Equations (2.2.1a) and (2.2.1b) are the Gauss's law for electric and magnetic field, respectively. The other two equations are Faraday's law (2.2.1c) and Ampere's law (2.2.1d), where $\mathbf{E}$ is the electric field in $[V/m]$, $\mathbf{H}$ is the magnetic field in $[A/m]$, $\mathbf{M}$ is the equivalent magnetic current density in $[V/m^2]$ and $\mathbf{J}$ is the electric current density in $[A/m^2]$.

For linear, isotropic and nondispersive media, we write constitutive relations to supplement Maxwell's equations and characterize the material response to electromagnetic fields. These constitutive relations can be written as [Jackson, 1998]

$$\mathbf{D} = \varepsilon_r \varepsilon_0 \mathbf{E} \tag{2.2.2a}$$

$$\mathbf{B} = \mu_r \mu_0 \mathbf{H} \tag{2.2.2b}$$

where, ε_r is the relative permittivity, $\varepsilon_0 \simeq 8.854 \cdot 10^{-12}\,[F/m]$ is the free space permittivity, μ_r is the relative permeability and $\mu_0 = 4\pi \cdot 10^{-7}\,[H/m]$ is the free space permeability.

The field densities $\mathbf{J}$ and $\mathbf{M}$ can act as independent sources of electric and magnetic fields respectively. For materials that are isotropic and have nondispersive electric and magnetic losses, we can write [Taflove A., 2005]

$$\mathbf{J} = \mathbf{J}_i + \sigma \boldsymbol{E} \tag{2.2.3a}$$

$$\mathbf{M} = \mathbf{M}_i + \sigma_m \mathbf{H} \tag{2.2.3b}$$

where, σ is the electric conductivity $[S/m]$ and σ_m is the equivalent magnetic loss $[\Omega/m]$, together with the impressed electric current density $\mathbf{J}_i$ and the equivalent impressed magnetic current density $\mathbf{M}_i$. In this Thesis, we do not work with magnetic materials thus $\mathbf{M}_i = 0$.

We just need to consider Faraday's and Ampere's laws in the FDTD method, because the divergence equations are automatically satisfied by the FDTD update equations.

For all of the vector components of the curl operator in Faraday's and Ampere's laws, we obtain six coupled scalar equations. For example, for the component z of the electric field in cartesian coordinates we have [Taflove A., 2005]

$$\frac{\partial E_z}{\partial t} = \frac{1}{\varepsilon_z}\left[\frac{\partial H_y}{\partial x} - \frac{\partial H_x}{\partial y} - (J_{zi} + \sigma E_z)\right]. \tag{2.2.4}$$

The relative permittivity ε_z is related with the electric field E_z through constitutive relations. The same holds for the other components of the electric fields. There is a similar relation between the relative permeability and magnetic field.

The rest of the five coupled scalar equations are given in the Ref.[Taflove A., 2005] (chapter 3, page 53).

The FDTD method divides the problem geometry into a spatial grid in which the electric and magnetic fields are placed at discrete points of the so called Yee cell. The fields are positioned in the Yee cell as shown in Figure (2.2.1). Each component of the magnetic field is surrounded by four electric field components. This configuration is due to Faraday's law. The same happens for the electric field due for Ampere's law. The FDTD method solves the resulting equations at discrete time instances, so we must approximate the time and space derivatives using finite differences, then calculate the values of fields at a future time from the field values in the past. For example, the discrete version of equation (2.2.4) becomes

$$\begin{aligned}\frac{E_z^{n+1}(i,j,k) - E_z^n}{\Delta t} = &\frac{1}{\varepsilon_z(i,j,k)}\frac{H_y^{n+\frac{1}{2}}(i,j,k) - H_y^{n-\frac{1}{2}}(i-1,j,k)}{\Delta x} \\ &- \frac{1}{\varepsilon_z(i,j,k)}\frac{H_x^{n+\frac{1}{2}}(i,j,k) - H_x^{n-\frac{1}{2}}(i,j-1,k)}{\Delta y} \\ &- \frac{\sigma_z(i,j,k)}{\varepsilon_z(i,j,k)} E_z^{n+\frac{1}{2}}(i,j,k) - \frac{1}{\varepsilon_z(i,j,k)} J_{iz}^{n+\frac{1}{2}}(i,j,k)\end{aligned} \tag{2.2.5}$$

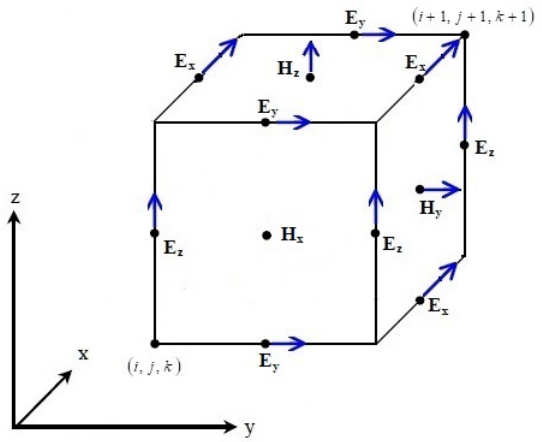

Figure 2.2.1: Shows a Yee cell between the nodes (i, j, k) and $(i + 1, j + 1, k + 1)$, how can be seen, the electric field is offset a half spatial step and the magnetic field is on the center of the face of the Yee cell.

where Δt is the temporal resolution and Δx and Δy are the spatial resolutions of the algorithm. As can be seen, the electric and magnetic fields are not sampled at the same time instants, the electric field is calculated at integer time steps and the magnetic field is calculated at half integer time steps, and they are offset from each other by $\Delta t/2$, accordingly the term $E_z^{n+\frac{1}{2}}(i, j, k)$, can be written as the average of the terms at integer time steps $(n + 1)\Delta t$ and $n\Delta t$, such that [Schneider, 2012]

$$E_z^{n+\frac{1}{2}}(i, j, k) = \frac{E_z^{n+1}(i, j, k) + E_z^n(i, j, k)}{2}. \tag{2.2.6}$$

It can be seen in equation (2.2.5), that the material parameters $(\epsilon_r, \mu_r, \sigma, \sigma_m)$ are associated with the fields components, so they are indexed with the same labels (i, j, k) in the six coupled equations.

Using the equations (2.2.5) and (2.2.6), we can arrange the terms such that the future field value $E_z^{n+1}(i, j, k)$ is kept on the left-hand side of the equation and the remaining terms are moved on
the right-hand side, giving a update equation of the form

$$\begin{aligned} E_z^{n+1}(i, j, k) &= C_{eze}(i, j, k) E_z^n(i, j, k) \\ &+ C_{ezhy}(i, j, k)\left(H_y^{n+\frac{1}{2}}(i, j, k) - H_y^{n-\frac{1}{2}}(i-1, j, k)\right) \\ &+ C_{ezhx}(i, j, k)\left(H_x^{n+\frac{1}{2}}(i, j, k) - H_x^{n-\frac{1}{2}}(i, j-1, k)\right) \\ &+ C_{ezj}(i, j, k) J_{iz}^{n+\frac{1}{2}}(i, j, k) \end{aligned} \tag{2.2.7}$$

where the update coefficients are given by

$$C_{eze}(i, j, k) = \frac{2\varepsilon_z(i, j, k) - \Delta t\sigma_z(i, j, k)}{2\varepsilon_z(i, j, k) + \Delta t\sigma_z(i, j, k)} \tag{2.2.8a}$$

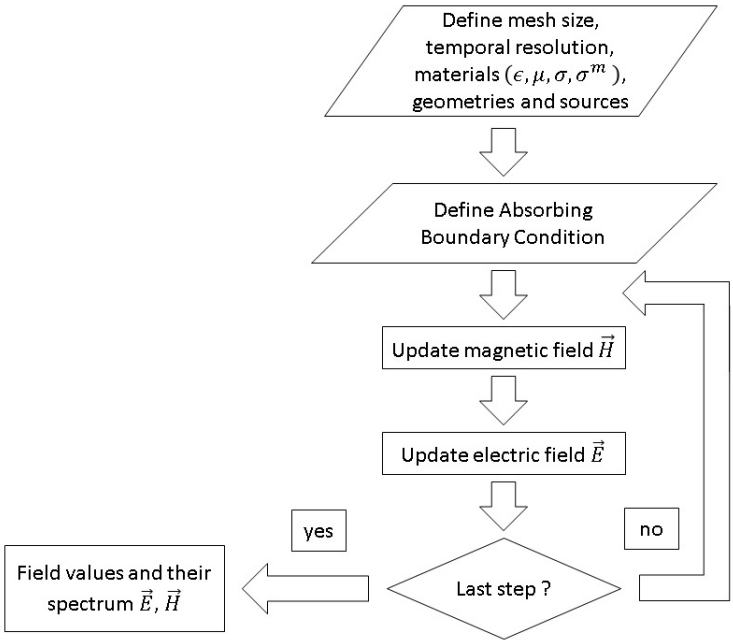

Figure 2.2.2: Shows the flow diagram of the FDTD method implemented in this Thesis.

$$C_{ezhy}(i,j,k) = \frac{2\Delta t}{(2\varepsilon_z(i,j,k) + \Delta t\sigma_z(i,j,k))\,\Delta x} \tag{2.2.8b}$$

$$C_{ezhx}(i,j,k) = -\frac{2\Delta t}{(2\varepsilon_z(i,j,k) + \Delta t\sigma_z(i,j,k))\,\Delta y} \tag{2.2.8c}$$

$$C_{ezj}(i,j,k) = -\frac{2\Delta t}{2\varepsilon_z(i,j,k) + \Delta t\sigma_z(i,j,k)} \tag{2.2.8d}$$

the subscript represents the field that it is being updated and the field that is being multipled. For example, the coefficient C_{ezhy} is updating the field E_z and is multiplying H_y.

The rest of the five update equation are given in the Ref.[Taflove A., 2005] (chapter 3, page 62).

After deriving the update equations for all the fields, an algorithm can be designed as shown in Figure (2.2.2). The first step within the algorithm is define the problem parameters, which cover the

types of materials related to the permittivity, permeability, electrical and magnetic conductivities, the geometry of the material, the source used, the update coefficients and the electric and magnetic fields. The second step is to define the parameters that make it possible for the wave incident is not reflected at the boundaries of the computational domain, where an Absorbing Boundary Condition (ABC) is used, the use of this method will be discussed in more detail in the Absorbing Boundary Conditions section. Already being in the algorithm cycle, during each time step it will calculate the future values of the fields, for a given time in the definition of problem parameters. Once the last iteration, the cycle stops and prints the output data, such as sampling the fields in the time domain at some node along with their respective spectrum of frequencies.

2.3 Numerical dispersion and stability in FDTD method

The FDTD algorithm computes the electric and magnetic fields in discrete points in space and time. Due to discretization, the curl equations (2.2.1c) and (2.2.1d), can result in nonphysical dispersion of waves in free space. That is, the phase velocity of numerical wave modes can differ from c, the speed of light in free space, by an amount that vary with the wavelength, direction of propagation and grid discretization. Therefore, the choise of the temporal resolution Δt and spatial resolutions Δx, Δy and Δz are not arbitrary. Certain requirements must be met in order to guarantee stability and accuracy of the results at the highest frequency of interest in the problem. In this section, we discuss conditions that give precise solutions obtained by the FDTD method.

2.3.1 Yee cell size

The size of the Yee cell is an important parameter that guarantees correct results over a wide range of frequencies. In general, it is desired that the shortest wavelength of the incident source be greater than the size of Yee cell. An often-quoted constraint is 20 cells per wavelength, which is necessary in applications as radar scattering cross sections [Kunz, 1993]. If the cell size is much smaller than the Nyquist sampling limit, $\lambda_{\min} = 2\Delta s$, where $\Delta s = \max[\Delta x, \Delta y, \Delta z]$ is the maximum of spatial resolutions, this choice gives reasonable results. The shortest wavelength is related with the spatial resolution according to

$$\lambda_{\min} = N_\lambda \Delta s \tag{2.3.1}$$

where N_λ are the cells per wavelength. For higher values of N_λ more RAM memory is required for a serial computer architecture, because the spatial resolution must be decreased.

2.3.2 Courant condition for optimal temporal resolution

The speed of light in free space is [Jackson, 1998]

$$c = \frac{1}{\sqrt{\varepsilon_0 \mu_0}}. \tag{2.3.2}$$

Ideally, this value must also be obtained inside of the computational domain. In one dimension it is easy to obtain a propagation speed equal to c, but in grids with two and three dimensions this is not possible due to the discretization of the method. We should consider how fast the wave must move at each time step $n\Delta t$. Taken to control of this phase velocity in higer dimensions, errors could occur due to numerical instability, making the fields to increase exponentially while the simulations runs.

To ensure the stability of the method, we use the Courant condition, which indicates the desired size of the temporal resolution. In three dimensions, the Courant condition is [Taflove A., 2005]

$$c\Delta t \leq \frac{1}{\sqrt{\frac{1}{\Delta x^2} + \frac{1}{\Delta y^2} + \frac{1}{\Delta z^2}}} \tag{2.3.3}$$

if we consider the practical case of a three dimensional cubic cell space lattice with $\Delta x = \Delta y =$

$\Delta z = \Delta$, then

$$\frac{c\Delta t}{\Delta} \leq S \tag{2.3.4}$$

where $S = \frac{1}{\sqrt{3}}$ is the Courant number for a cubic cell lattice. In all calculations of this Thesis, the Courant number was set to 90% of its upper bound. Even when the results are correct, making the temporary resolution Δt smaller does not guarantee more accurate results, due to the intrinsic dispersion of the grid.

2.3.3 Numerical dispersion

Numerical dispersion is an error in the propagation of electromagnetic waves in the grid, associated with a nonphysical phase velocity due to the discretization. The shape of the incident wave suffers a distortion, because the phase velocity is different for each frequency component and therefore is different from the continuous case c/n, where n is the refractive index of the medium. In the computational domain, the value of the phase velocity changes by the spatial resolution and the direction of propagation. In the continuous case, the dispersion relation in vacuum is given by [Jackson, 1998]

$$\left(\frac{\omega}{c}\right)^2 = k_x^2 + k_y^2 + k_z^2 \tag{2.3.5}$$

where ω is the angular frequency and k_x, k_y and k_z are the wave numbers for each component of the propagation. In the computational domain, the dispersion relation is instead given by [Taflove A., 2005]

$$\left(\frac{\omega}{2c} sinc\left(\frac{\omega\Delta t}{2}\right)\right)^2 = \left(\frac{k_x}{2} sinc\left(\frac{k_x\Delta x}{2}\right)\right)^2 + \left(\frac{k_y}{2} sinc\left(\frac{k_y\Delta y}{2}\right)\right)^2 + \left(\frac{k_z}{2} sinc\left(\frac{k_z\Delta z}{2}\right)\right)^2 \tag{2.3.6}$$

where $sinc\,(x) = {}^{\sin(x)}/_{x}$, represent the sinc function. We can see that in the limit ${}^{\Delta t}/_{2} \to 0$, ${}^{\Delta x}/_{2} \to 0$, ${}^{\Delta y}/_{2} \to 0$ and ${}^{\Delta z}/_{2} \to 0$, we obtain equation (2.3.5). This means that the errors produced by numerical dispersion are reduced when the temporal and the spatial resolutions are increased. However, using a finer grid implies a greater use of RAM memory and calculation time.

It can also be shown that equation (2.3.6) reduces to (2.3.5) if the Courant number and the direction of wave propagation are suitable chosen. For example, reduction to the continuous dispersion case results for a numerical plane wave propagating along a diagonal of a three dimensional cubic lattice $k_x = k_y = k_z = Sk$, where S is the Courant number.

In general, the phase velocity changes as a function of the incident angles inside of the computational domain. We can take as an example, a two dimensional grid as shown in Figure (2.3.1), where it is observed that for $N_\lambda = 20$ cells per wavelength, it is possible to obtain accurate results independently of the incident angle and without the need to use a finer grid. Consequently, although errors due to numerical dispersion are always present, these can be controlled.

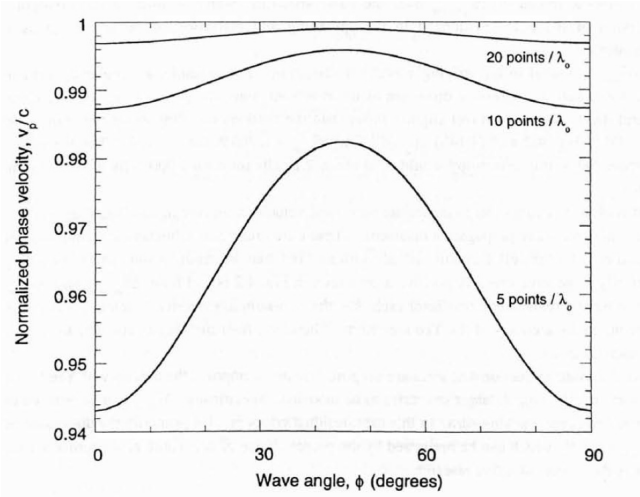

Figure 2.3.1: Variation of numerical phase velocity with wave propagation angle in a two dimensional FDTD method, the grid used for three sampling densities of the square unit cells. $S = 0.5$ for all of the cases. Taken from Ref.[Taflove A., 2005].

2.4 Field sources in the FDTD method

The use of sources in FDTD problems is an important concept and necessary to carry out simulations. There are two methods to implement sources in the FDTD method, near zone sources, such as voltage and current sources [Tirkas P. A., 1992] and far zone sources such as plane waves in scattering problems [Sepulveda, 2017].

A pulse source excites both electric and magnetic fields with a waveform as a function of time, that can be specific to the problem under consideration, taking into consideration, the range of the frequencies of interest in the problem.

The infinitesimal current element is a useful type of source, because it is possible to use in modeling radiating dipoles or monopoles [Tirkas P. A., 1992], optical emission from fluorescent molecules [Buechler et al., 1995], and quantum dots in inhomogeneous environments. It can be used for analyzing spontaneous emission [Vuckovic et al., 2000], Casimir force [Atkins et al., 2012], solar cells [Callahan et al., 2012] and so on.

In this Thesis, we work with near zone sources to implement an infinitesimal current element source, that can vary in time along a directed line of infinitesimal length in some axis.

2.4.1 Electric dipole model

We already mentioned that the FDTD method solves Faraday's and Ampere's laws in the time domain and we do not need to solve directly the Gauss's laws for this implementation, because equation (2.2.1b) will be zero at any time later. In others words, the divergence equation is indirectly

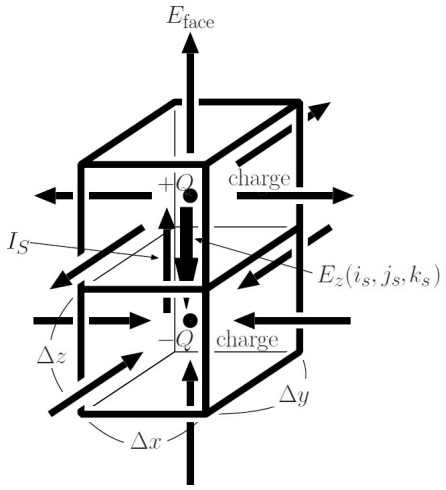

Figure 2.4.1: Charges and fields generated in two contiguous Yee cells by a current impressed at a FDTD node as a point source. Taken from Ref.[Costen F., 2009].

fulfilled and the time evolution for the equation (2.2.1a) holds at every space location [Pontalti et al., 2002]

$$(\boldsymbol{\nabla} \cdot \boldsymbol{D})_t = -\int_0^t (\boldsymbol{\nabla} \cdot \boldsymbol{J}_i)_{t'}\, dt' \tag{2.4.1}$$

thus, the equation (2.4.1) may be different from zero at time t if the integral on the right hand side does not vanish. This equation indicates the way in which free charges are introduced by the FDTD method, without explicitly using a charge density function. In the curl equations, in fact, the only allowed physical sources are currents.

To radiate a wave from a single point $(i_s\Delta x, j_s\Delta y, k_s\Delta z)$, is needed to place a Hertzian dipole antenna at a some point of the grid by a impressing a current, which flows over a length l, as shown in Figure (2.4.1). This length l is usually much smaller than the cell size and must also be much smaller than $\lambda_{\min}$, where $\lambda_{\min}$ is the shortest wavelength of the source fields. The current density for this dipole is centered at the corresponding electric field node and is given by [Buechler et al., 1995]

$$J_{iz}^{n+\frac{1}{2}}(i_s, j_s, k_s) = \left(\frac{l}{\Delta x \Delta y \Delta z}\right) I_{iz}\left(t_{n+\frac{1}{2}}\right) \tag{2.4.2}$$

where I_{iz} is a function of time (source waveform), the line current is transformed to an equivalent volumetric current density averaged over one unit cell, then, this current density can be implemented in equation (2.2.7). However, some limitations of the FDTD method should be kept in mind while constructing the source waveforms to obtain a valid and accurate simulation result.

One of the considerations for the source waveform construction is its frequency. A temporal waveform is the sum of time-harmonic waveforms with a spectrum of frequencies that can be obtained using the Fourier transform. With this considerations I_{iz} can be a sinusoidal waveform, Gaussian waveform, normalized derivative of a Gaussian waveform or a cosine modulated Gaussian waveform for a desired frequency spectrum.

Test parameters	
Domain size $[\mu m^3]$	$1.2 \times 1.2 \times 1.2$
Computational Space, vacuum	$\epsilon_r = 1$, $\mu_r = 1$
Cell size $[nm]$	10
Maximum frequency $[THz]$	1499
Cells per wavelength at the maximum frequency	20
τ $[fs]$	0.336
t_0 time shift $[fs]$	1.667
Field probes $[nm]$	60, 200, 340

Table 2.4.1: Parameters for dipole emission simulation in FDTD.

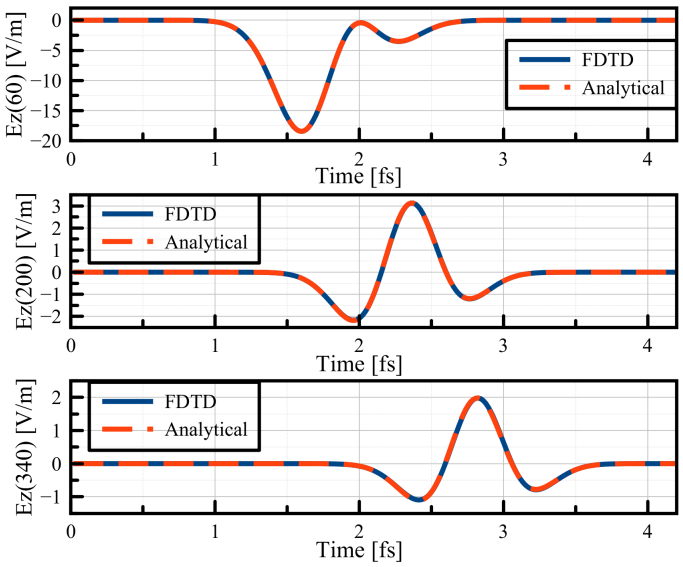

Figure 2.4.2: Electric field results for three distances from the source in 60 $[nm]$, 200 $[nm]$ and 340 $[nm]$ for both FDTD (blue) and analytical (red).

The fields radiated by the Hertzian dipole can be obtained with the FDTD method and through the analytical solution, which is given by [Xu, 2014]

$$E_z(r,t) = \frac{-\eta_0}{4\pi r}\left[\frac{p_z\left(t-\frac{r}{c}\right)}{r} + \frac{1}{c}\frac{\partial}{\partial t}p_z\left(t-\frac{r}{c}\right) + \frac{c}{r^2}\int_0^t p_z\left(t'-\frac{r}{c}\right)dt'\right] \tag{2.4.3}$$

where r is the distance from the source and $p_z = lI_z$ is the instantaneous dipole moment.

For the FDTD simulations in this Thesis, we use the derivative Gaussian waveform

$$I_{iz}(t) = \frac{-\sqrt{2e}}{\tau}(t-t_0)\, e^{-\left(\frac{t-t_0}{\tau}\right)^2} \tag{2.4.4}$$

with the parameters given in Table (2.4.1), chosen to compare the analytical and the FDTD results in the time domain.

Figure (2.4.2) shows that the agreement is good between the analytical and numerical result.

2.5 Absorbing Boundary Conditions

Because the computational capacity and RAM memory size is finite, the computational space needs to be truncated using special boundary conditions. In many applications, such as radiation scattering problems, the boundaries need to simulate open space [Taflove A., 2005]. One conceptually simple approach to simulate an open space consists in terminating outer boundaries of the space grid with an absorbing material. Ideally, this medium should be only a few lattice cells thick and reflectionless to all impinging waves over their full frequency spectrum, highly absorbing and effective in the near field of a source or a scatterer. In other words, any waveform that reaches the absorbing boundary condition is unable to reflect back into the computational space.

There are several methods to implement this kind of Absorbing Boundary Conditions (ABC) [Mur, 1981, Mei K. K., 1992, Berenger, 2007], but the most useful for absorbing evanescent waves is the Convolution Perfectly Matched Layer method (CPML) [Roden J. A., 2000], which can absorb waves in isotropic and homogeneous media, but also, in inhomogeneous, lossy, dispersive, anisotropic or nonlinear media. This application is completely independent of the host medium. The efficient implementation of a CPML has been widely used and incorporated into a number of commercial FDTD software packages.

The method is based in the Perfectly Matched Layer technique (PML) [Berenger, 2007], that uses fictitious constitutive parameters (σ, σ_m) to create a wave impedance matching condition, which is independent of the angles and frequencies of the wave incident on the boundary.

2.5.1 Formulation of CPML

Without loss of generality, the PML equations for a lossy medium are given for the z component of the electric field in the frequency domain [Roden J. A., 2000]

$$i\omega\epsilon_z E_z + \sigma_z E_z = \frac{1}{S_{ex}}\frac{\partial H_y}{\partial x} - \frac{1}{S_{ey}}\frac{\partial H_x}{\partial y} \tag{2.5.1}$$

where S_{ex} and S_{ey} are the stretched coordinate metrics and they are given by

$$S_{ej} = 1 + \frac{\sigma_j}{i\omega\epsilon_0} \tag{2.5.2}$$

for $j = x, y, z$. Following the definition proposed by Kuzuoglu and Mittra [Kuzuoglu M., 1996], we can write

$$S_{ej} = \kappa_{ej} + \frac{\sigma_{pj}}{\alpha_{ej} + i\omega\epsilon_0} \tag{2.5.3}$$

where α_{ej} and σ_{pj} are assumed to be positive and real and κ_{ej} is real and ≥ 1. In the time domain, equation (2.5.1) is given by

$$\epsilon_z \frac{\partial E_z}{\partial t} + \sigma_z E_z = \overline{S}_{ex} * \frac{\partial H_y}{\partial x} - \overline{S}_{ey} * \frac{\partial H_x}{\partial y} \tag{2.5.4}$$

where $\overline{S}_{ex}$ and $\overline{S}_{ey}$ are the inverse Laplace transform of S_{ex}^{-1} and S_{ey}^{-1} respectively. In the time domain, the product operation in equation (2.5.1) is expressed as convolution operations (2.5.4).

It can be shown that $\overline{S}_{ej}$ has the impulse response

$$\overline{S}_{ej} = \frac{\delta(t)}{\kappa_{ej}} - \frac{\sigma_{pj}}{\epsilon_0 \kappa_{ej}^2} e^{-\left(\frac{\sigma_{pj}}{\epsilon_0 \kappa_{ej}} + \frac{\alpha_{pj}}{\epsilon_0}\right) t} u(t) \tag{2.5.5}$$

where $\delta(t)$ is the unit impulse function and $u(t)$ is the unit step function. Inserting equation (2.5.5) into (2.5.4) leads to

$$\epsilon_z \frac{\partial E_z}{\partial t} + \sigma_z E_z = \frac{1}{\kappa_{ex}} \frac{\partial H_y}{\partial x} - \frac{1}{\kappa_{ey}} \frac{\partial H_x}{\partial y} + \xi_{ex}(t) * \frac{\partial H_y}{\partial x} - \xi_{ey}(t) * \frac{\partial H_x}{\partial y} \tag{2.5.6}$$

where

$$\xi_{ej}(t) = -\frac{\sigma_{pj}}{\epsilon_0 \kappa_{ej}^2} e^{-\left(\frac{\sigma_{pj}}{\epsilon_0 \kappa_{ej}} + \frac{\alpha_{pj}}{\epsilon_0}\right) t} u(t) \tag{2.5.7}$$

for $j = x, y, z$. Equation (2.5.7) represents an exponential, decay of the wave as it penetrates the absorbing boundary.

The central difference approximation can be used to express equation (2.5.6) in discrete time and space, and then obtain a modified field update equation for E_z^{n+1}. The two convolution terms also need to be expressed in discrete time and space before proceeding with the construction of the update equations. To do this, we can use the recursive convolution method presented in Ref.[Beggs et al., 1992] and a set of auxiliary expressions ψ_i. Then, we can calculate for the $\pm x$ and $\pm y$ boundaries [Roden J. A., 2000]

$$\psi_{ezx}^{n+\frac{1}{2}}(i,j,k) = b_{ex} \psi_{ezx}^{n-\frac{1}{2}}(i,j,k) + a_{ex} \left(H_y^{n+\frac{1}{2}}(i,j,k) - H_y^{n+\frac{1}{2}}(i-1,j,k) \right) \tag{2.5.8a}$$

$$\psi_{ezy}^{n+\frac{1}{2}}(i,j,k) = b_{ey} \psi_{ezy}^{n-\frac{1}{2}}(i,j,k) + a_{ey} \left(H_x^{n+\frac{1}{2}}(i,j,k) - H_x^{n+\frac{1}{2}}(i,j-1,k) \right) \tag{2.5.8b}$$

where

$$a_{ej} = \frac{\sigma_{pj}}{\Delta j \left(\sigma_{pj} \kappa_{ej} + \alpha_{ej} \kappa_{ej}^2 \right)} (b_{ej} - 1) \tag{2.5.9a}$$

$$b_{ej} = e^{-\left(\frac{\sigma_{pj}}{\kappa_{ej}} + \alpha_{ej}\right) \frac{\Delta t}{\epsilon_0}} \tag{2.5.9b}$$

for $j = x, y, z$. Then, we can add the equations (2.5.8a) and (2.5.8b) to the usual field update equation (2.2.7) in the CPML regions to read

$$E_z^{n+1}(i,j,k) = E_z^{n+1}(i,j,k) + C_{\psi ezx}(i,j,k) \psi_{ezx}^{n+\frac{1}{2}}(i,j,k) + C_{\psi ezy}(i,j,k) \psi_{ezy}^{n+\frac{1}{2}}(i,j,k) \tag{2.5.10}$$

where $C_{\psi ezx}(i,j,k) = \Delta x C_{ezhy}(i,j,k)$ and $C_{\psi ezy}(i,j,k) = \Delta y C_{ezhx}(i,j,k)$, at the boundaries $\pm x$ and $\pm y$. The updating coefficient are given by

$$C_{ezhy}(i,j,k) = \frac{1}{\kappa_{ex}} C_{ezhy}(i,j,k) \tag{2.5.11a}$$

$$C_{ezhx}(i,j,k) = \frac{1}{\kappa_{ey}} C_{ezhx}(i,j,k). \tag{2.5.11b}$$

This scheme is second order accurate, and is stable within the Courant limit for all possitive α_{ej} and σ_{pj} and for all real values $\kappa_{ej} \geq 1$.

The same procedure is implemented for the magnetic field, where the impulse response is given by

$$\overline{S}_{mj} = \frac{\delta(t)}{\kappa_{mj}} - \frac{\sigma_{pmj}}{\epsilon_0 \kappa_{mj}^2} e^{-\left(\frac{\sigma_{pmj}}{\epsilon_0 \kappa_{mj}} + \frac{\alpha_{pmj}}{\epsilon_0}\right)t} u(t) \tag{2.5.12}$$

and α_{pmj}, σ_{pmj} are assumed to be positive and real and κ_{mj} is real and ≥ 1.

In this Thesis, we use the parameters reported in Ref.[Roden J. A., 2000].

2.6 Dispersive Material

In many problems, one can obtain fairly accurate results by assuming that the material parameters are constants over the frequency band of interest. However, constant materials parameters are an approximation. For example, it is impossible to have a lossless dielectric with constant permittivity (except free space). The FDTD method allows modeling the behavior of complex media such as dispersion and nonlinearity. It is possible develop accurate algorithms that can model the electromagnetic properties of these media and integrate this methods within the discrete time domain solution.

When the speed of light in a material is a function of frequency, the material is said to be dispersive. The fact is that the FDTD method can introduce numerical dispersion has been discussed in the section 3. In that case, dispersion is a numerical artifact and is distinct from the subject of this section.

Dispersion modeling has been introduced in many algorithms, most of these are classified Z-transform technique [Sullivan, 1992], recursive convolution method (RC) [Kelley D. F., 1996] and the auxiliary differential equation (ADE) [Takayama Y., 2002]. A review of these techniques is presented in Ref.[Teixeira, 2008].

For dispersive materials, some models that can simulate the relevant dependence of frequency include the Debye, Drude and Lorentz models. The Debye model is commonly used to approximate the frequency behavior of biological tissues, the Lorentz model describes some metamaterials such as Double-Negative index media close to resonances and Drude model is useful in describing the behavior of metals at optical frequencies [Teixeira, 2008].

The ADE method uses a time domain auxiliary differential equation linking either the electric current density or the polarization.The difference between these two forms lies in the number of stored variables and in accuracy. In this Thesis, we use the formalism with polarization (ADE).

2.6.1 Drude Materials

The permittivity of a multipole Drude material can be described as [Okoniewski M., 2006]

$$\epsilon(\omega) = \epsilon_0 \epsilon_\infty - \sum_{1}^{N_p} \frac{\epsilon_0 \omega_p^2}{\omega^2 - i\omega\gamma_p} \tag{2.6.1}$$

where p denotes the number of the Drude poles, ϵ_∞ is the infinite permittivity, ω_p is the plasma frequency and γ_p is the inverse of the pole relaxation time. Ampere's law with the polarization term is given by [Ammann, 2007]

$$\boldsymbol{\nabla} \times \mathbf{H} = \epsilon_0 \epsilon_\infty \frac{\partial \mathbf{E}}{\partial t} + \sigma \mathbf{E} + \sum_{1}^{N_p} \frac{\partial \mathbf{P}_p}{\partial t} \tag{2.6.2}$$

where $\mathbf{P}_p$ satisfied the following differential equation

$$-\frac{d^2}{dt^2}\mathbf{P}_p - \gamma_p \frac{d}{dt}\mathbf{P}_p = \omega_p^2 \epsilon_0 \mathbf{E}. \tag{2.6.3}$$

Equation (2.6.3) can now be discretized to get the update equation using the standard central difference scheme

$$\mathbf{P}_p^{n+1} = C_{qq}\mathbf{P}_p^n + C_{qqm}\mathbf{P}_p^{n-1} + C_{qe}\mathbf{E}_p^n \tag{2.6.4}$$

where the updating coefficients are given by

$$C_{qq} = \frac{4}{\gamma_p \Delta t + 2} \tag{2.6.5a}$$

$$C_{qqm} = \frac{\gamma_p \Delta t - 2}{\gamma_p \Delta t + 2} \tag{2.6.5b}$$

$$C_{qe} = \frac{2\epsilon_0 \Delta t^2 \omega_p^2}{\gamma_p \Delta t - 2}. \tag{2.6.5c}$$

Then, the field update equation for E_z^{n+1} in a dispersive material becomes

$$\begin{aligned} E_z^{n+1}(i,j,k) &= C_{eze}(i,j,k)\, E_z^n(i,j,k) \\ &+ C_{ezhy}(i,j,k)\left(H_y^{n+\frac{1}{2}}(i,j,k) - H_y^{n-\frac{1}{2}}(i-1,j,k)\right) \end{aligned} \tag{2.6.6}$$

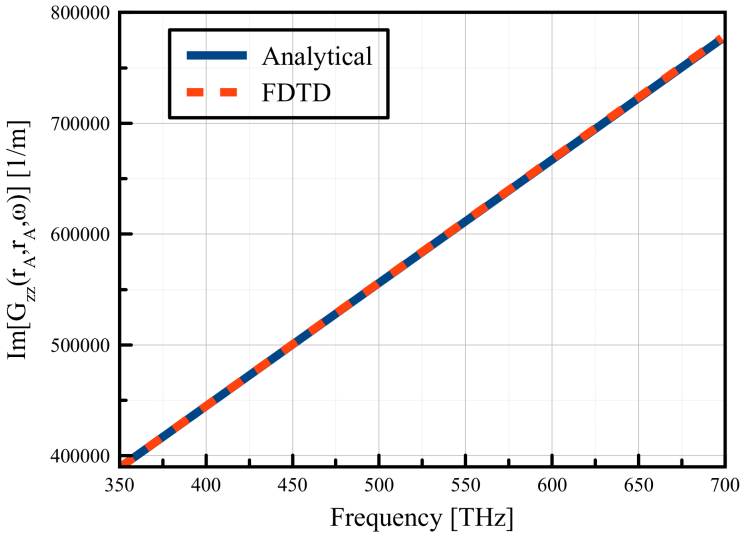

Figure 2.6.1: Comparison between the imaginary part of the Green's function in vacuum, obtained analytically (blue line) and numerically with FDTD method (red line) using 3000 time steps.

$$+C_{ezhx}\left(i,j,k\right)\left(H_x^{n+\frac{1}{2}}\left(i,j,k\right)-H_x^{n-\frac{1}{2}}\left(i,j-1,k\right)\right)$$

$$+C_{ezj}\left(i,j,k\right)J_{iz}^{n+\frac{1}{2}}\left(i,j,k\right)-\frac{\Delta x}{\Delta t}C_{ezhy}\left(i,j,k\right)\sum_{1}^{N_p}\left(P_{p,z}^{n+1}-P_{p,z}^{n}\right)$$

the updating coefficients are the same for the nondispersive case.

2.7 Homogeneous Green's function in free space

The full dipole numerical calculation of the Green's function are performed using the integral volume equation

$$\mathbf{E}\left(\mathbf{r},\omega\right)=j\mu_0\mu_r\omega\int_{V'}\overleftrightarrow{\mathbf{G}}\left(\mathbf{r},\mathbf{r}';\omega\right)\mathbf{J}\left(\mathbf{r}',\omega\right)dV' \tag{2.7.1}$$

the response of the system to a polarization source by a point dipole at $\mathbf{r}'$ is

$$\mathbf{J}\left(\mathbf{r}',\omega\right)=\mathbf{J}\left(\omega\right)\delta\left(\mathbf{r}-\mathbf{r}'\right) \tag{2.7.2}$$

where $\mathbf{J}\left(\omega\right)$ is the current density source. This reduce equation (2.7.1) to [Taflove A., 2013]

$$\mathbf{E}\left(\mathbf{r},\omega\right)=j\mu_0\mu_r\omega\Delta x\Delta y\Delta z\overleftrightarrow{\mathbf{G}}\left(\mathbf{r},\mathbf{r}';\omega\right)\mathbf{J}\left(\omega\right). \tag{2.7.3}$$

The total Green's function for a given polarization of the source is [Vlack, 2012, Cartar, 2017]

$$G_{nm}\left(\mathbf{r},\mathbf{r}',\omega\right)=\frac{1}{i\mu_0\mu_r\omega\Delta x\Delta y\Delta z}\frac{E_n\left(\mathbf{r},\omega\right)}{J_m\left(\omega\right)} \tag{2.7.4}$$

where $n,m=x,y,z$. If we wish to change the initial dipole orientation or the initial dipole position

$\mathbf{r}'$, we must recalculate the time dependent fields E_n, to obtain more components of the Green's tensor.

The best results for these Green's function are giving when the simulations are run extremely long times, such that the initial signal has decayed to 10^{-5} of its original value, and the bandwidth of the pulse covering properly the frequency range of interest [Vlack, 2012].

Unfortunately, such direct numerical technique is computationally expensive, since each simulations only defines one component of the Green's tensor at specific localization $\mathbf{r}$ and $\mathbf{r}'$.

We can obtain the imaginary part of Green's function in vacuum with the FDTD method and compare with the analytical solution in $\mathbf{r}_A = \mathbf{r}' = 0$. The result of the simulation are shown in Figure (2.6.1), where the analytical result is

$$\mathrm{Im}\left[G_{zz}\left(0,0,\omega\right)\right] = \frac{\omega}{6\pi c} \tag{2.7.5}$$

we can see a good agreement across the full spectrum of the source.

Chapter 3

Light-matter interaction in the near field with macroscopic QED

3.1 Quantization of the electric field

It is well known that the quantum statistical properties of the vacuum fluctuations of electromagnetic fields, including their interactions with atomic systems, can be strongly influenced by the presence of dielectric bodies. Examples of this are the Casimir effect [Milton, 2003], the modification of the spontaneous emission rate of excited atoms in presence of dielectric media [Jones et al., 2018] and the degradation or improvement of nonclassical properties of light propagating through optical devices, such as cavities, beam splitters, wave guides, which typically can be regarded as dielectric bodies [Knoll et al., 2000].

In order to arrive at the basic concepts for describing the quantum effects of radiation in real media, it is necessary to consider the quantization of the electromagnetic field attributed to atomic sources in presence of macroscopic bodies. The formalism enables us to take into account absorption and dispersion in a consistent way.

In presence of media, the equation of motion for the quantum electromagnetic field must be the same as the classical Maxwell's equations. The constitutive relations must also hold. The quantum fluctuations of the electromagnetic field must obey the fluctuation dissipation theorem. In a medium, one also has to distinguish between electric and magnetic field excitations.

In frequency domain, the electromagnetic field obeys Maxwell's equations [Buhmann, 2012]

$$\boldsymbol{\nabla} \cdot \hat{\mathbf{D}}(\mathbf{r}, \omega) = \hat{\rho}_N \tag{3.1.1a}$$

$$\boldsymbol{\nabla} \cdot \hat{\mathbf{B}}(\mathbf{r}, \omega) = 0 \tag{3.1.1b}$$

$$\boldsymbol{\nabla} \times \hat{\mathbf{E}}(\mathbf{r}, \omega) - i\omega \hat{\mathbf{B}}(\mathbf{r}, \omega) = 0 \tag{3.1.1c}$$

$$\boldsymbol{\nabla} \times \hat{\mathbf{H}}(\mathbf{r}, \omega) + i\omega \hat{\mathbf{D}}(\mathbf{r}, \omega) = \mu_0 \hat{\mathbf{J}}_N \tag{3.1.1d}$$

where $\hat{\mathbf{E}}$ and $\hat{\mathbf{H}}$ are the electric and magnetic field operators, $\hat{\mathbf{D}}$ and $\hat{\mathbf{B}}$ are the electric and magnetic flux operators respectively, ω is the frequency, $\hat{\rho}_N$ is the charge density operator and $\hat{\mathbf{J}}_N$ is the current density operator. The constitutive relations that characterize, linear and isotropic media

read

$$\hat{\mathbf{D}}(\mathbf{r},\omega) = \epsilon_0 \epsilon_r(\mathbf{r},\omega)\,\hat{\mathbf{E}}(\mathbf{r},\omega) + \hat{\mathbf{P}}_N(\mathbf{r},\omega) \tag{3.1.2a}$$

$$\hat{\mathbf{H}}(\mathbf{r},\omega) = \frac{1}{\mu_0 \mu_r(\mathbf{r},\omega)}\hat{\mathbf{B}}(\mathbf{r},\omega) - \hat{\mathbf{M}}_N(\mathbf{r},\omega). \tag{3.1.2b}$$

where ϵ_0, μ_0 are the vacuum permittivity and the permeability, respectively, and ϵ_r, μ_r are the relative material permittivity and permeability.

From statistical mechanics it is clear that dissipation is unavoidably connected with the appearance of a random force that gives rise to an additional noise source on the electromagnetic field. Such a model leads to an energy flow essentially only in one direction, namely from the medium to the reservoir where it becomes absorbed. The quantum noise polarization and magnetization are related to the corresponding noise charge and current densities according to the continuity equation for charge and current given by

$$\hat{\mathbf{J}}_N(\mathbf{r},\omega) = -i\omega\hat{\mathbf{P}}_N(\mathbf{r},\omega) + \boldsymbol{\nabla}\times\hat{\mathbf{M}}_N(\mathbf{r},\omega) \tag{3.1.3a}$$

$$i\omega\hat{\rho}_N(\mathbf{r},\omega) = \boldsymbol{\nabla}\cdot\hat{\mathbf{J}}_N(\mathbf{r},\omega) \tag{3.1.3b}$$

Since the noise fields are quantum operators, we must specify their commutation relations. The choice should be such that noise polarization and magnetization vanish on their quantum average and that their fluctuation spectrum obeys the fluctuation-dissipation theorem. These conditions can be fulfilled by relating polarization and magnetization to a continuum set of fundamental annihilation and creation bosonic operators $\hat{\mathbf{f}}_\lambda(\mathbf{r},\omega)$ and $\hat{\mathbf{f}}^\dagger_\lambda(\mathbf{r},\omega)$, which play the role of the fundamental variables of the electromagnetic field in the dielectric medium [Buhmann, 2012]

$$\hat{\mathbf{P}}_N(\mathbf{r},\omega) = i\sqrt{\frac{\hbar\epsilon_0}{\pi}\mathrm{Im}\left[\epsilon_\mathrm{r}(\mathbf{r},\omega)\right]}\hat{\mathbf{f}}_e(\mathbf{r},\omega) \tag{3.1.4a}$$

$$\hat{\mathbf{M}}_N(\mathbf{r},\omega) = \sqrt{\frac{\hbar}{\pi\mu_0}\frac{\mathrm{Im}\left[\mu_\mathrm{r}(\mathbf{r},\omega)\right]}{|\mu_\mathrm{r}(\mathbf{r},\omega)|^2}}\hat{\mathbf{f}}_m(\mathbf{r},\omega) \tag{3.1.4b}$$

which obey bosonic commutation relations

$$\left[\hat{\mathbf{f}}_\lambda(\mathbf{r},\omega), \hat{\mathbf{f}}_{\lambda'}(\mathbf{r}',\omega')\right] = \left[\hat{\mathbf{f}}^\dagger_\lambda(\mathbf{r},\omega), \hat{\mathbf{f}}^\dagger_{\lambda'}(\mathbf{r}',\omega')\right] = \mathbf{0} \tag{3.1.5a}$$

$$\left[\hat{\mathbf{f}}_\lambda(\mathbf{r},\omega), \hat{\mathbf{f}}^\dagger_{\lambda'}(\mathbf{r}',\omega')\right] = \delta_{\lambda\lambda'}\delta(\omega-\omega')\,\boldsymbol{\delta}(\mathbf{r}-\mathbf{r}') \tag{3.1.5b}$$

where $\lambda, \lambda' \in \{e, m\}$. They represent the collective bosonic excitations of the lossy electromagnetic field of a given material structure. These modes are obtained by diagonalizing a Hamiltonian that includes both the electromagnetic excitations and a bath of harmonic oscillators, that describes the mechanisms responsible for the dissipation in the metal as already mentioned in Ref.[Huttner B., 1992].

In complete analogy to the classical case, we can combine equations (3.1.1c) and (3.1.1d), into a Helmholtz equation for the electric field operator

$$\left[\boldsymbol{\nabla}\times\boldsymbol{\nabla}\times-k_0^2\epsilon_r\left(\mathbf{r},\omega\right)\right]\hat{\mathbf{E}}\left(\mathbf{r},\omega\right)=i\omega\mu_0\hat{\mathbf{J}}_N\left(\mathbf{r},\omega\right) \tag{3.1.6}$$

where $k_0^2=\omega^2\epsilon_0\mu_0$ is the vacuum wave number. The corresponding Green's tensor equation reads

$$\left[\boldsymbol{\nabla}\times\boldsymbol{\nabla}\times-k_0^2\epsilon_r\left(\mathbf{r},\omega\right)\right]\overleftrightarrow{\mathbf{G}}\left(\mathbf{r},\mathbf{r}';\omega\right)=\overleftrightarrow{\mathbf{I}}\delta\left(\mathbf{r}-\mathbf{r}'\right) \tag{3.1.7}$$

where $\overleftrightarrow{\mathbf{I}}$ is the unit tensor, together with the boundary conditions

$$\overleftrightarrow{\mathbf{G}}\left(\mathbf{r},\mathbf{r}';\omega\right)\to 0\qquad\left|\mathbf{r}-\mathbf{r}'\right|\to\infty. \tag{3.1.8}$$

In vacuum using the vectorial identity $\left(\boldsymbol{\nabla}\times\boldsymbol{\nabla}\times\mathbf{A}=-\nabla^2\mathbf{A}+\boldsymbol{\nabla}\,\boldsymbol{\nabla}\cdot\mathbf{A}\right)$ in equation (3.1.6) write $\boldsymbol{\nabla}\cdot\mathbf{E}=\boldsymbol{\nabla}\cdot\mathbf{J}/i\omega\epsilon_0$, we obtain

$$\left[\nabla^2+k_0^2\epsilon_r\left(\mathbf{r},\omega\right)\right]\hat{\mathbf{E}}\left(\mathbf{r},\omega\right)=-i\omega\mu_0\left(\overleftrightarrow{\mathbf{I}}+\frac{\boldsymbol{\nabla}\boldsymbol{\nabla}}{k_0^2}\right)\cdot\hat{\mathbf{J}}_N\left(\mathbf{r},\omega\right) \tag{3.1.9}$$

then, we can write the solution for the electric field, assuming that the observation point is outside of the source region as

$$\hat{\mathbf{E}}\left(\mathbf{r},\omega\right)=i\omega\mu_0\int_{V'}d\mathbf{r}'g\left(\mathbf{r},\mathbf{r}'\right)\left(\overleftrightarrow{\mathbf{I}}+\frac{\boldsymbol{\nabla}\boldsymbol{\nabla}}{k_0^2}\right)\cdot\hat{\mathbf{J}}_N\left(\mathbf{r}',\omega\right) \tag{3.1.10}$$

where $g\left(\mathbf{r},\mathbf{r}'\right)=\frac{e^{ik_0R}}{4\pi R}$ is the scalar Green's function (Appendix A) and $R=\left|\mathbf{r}-\mathbf{r}'\right|$.

In vacuum the solution of equation (3.1.7) is the homogeneous Green's tensor given by

$$\overleftrightarrow{\mathbf{G}}^0\left(\mathbf{r},\mathbf{r}';\omega\right)=\left(\overleftrightarrow{\mathbf{I}}+\frac{\boldsymbol{\nabla}\boldsymbol{\nabla}}{k_0^2}\right)\frac{e^{ik_0R}}{4\pi R}. \tag{3.1.11}$$

Equation (3.1.11) is the general solution for a 3D homogeneous space and includes information about all possible linear events in the propagation of light, and many useful properties of a system can be found such as mode coupling, the light emission spectrum, the spontaneous emission enhancement factor and the local density of the states (LDOS). However, we are mostly interested in the Green's tensor where $\mathbf{r}=\mathbf{r}'$, we can rewrite the equation (3.1.11) in the form

$$\overleftrightarrow{\mathbf{G}}^0\left(\mathbf{r},\mathbf{r}';\omega\right)=\frac{e^{ik_0R}}{4\pi R}\left[\left(1+\frac{ik_0R-1}{k_0^2R^2}\right)\overleftrightarrow{\mathbf{I}}+\frac{3-3ik_0R-k^2R^2}{k_0^2R^2}\frac{\mathbf{RR}}{R^2}\right]. \tag{3.1.12}$$

We can begin by examining the limit $R\to 0$, which reads

$$\overleftrightarrow{\mathbf{G}}^0\left(\mathbf{r},\mathbf{r}';\omega\right)|_{\mathbf{r}\to\mathbf{r}'}=\frac{1}{4\pi}\left[\frac{2}{k_0^2R^2}+\frac{1}{R}+\frac{2ik_0}{3}+\cdots\right]\overleftrightarrow{\mathbf{I}} \tag{3.1.13}$$

then

$$\overleftrightarrow{\mathbf{G}}^0\left(0,\omega\right)|_{\mathbf{r}\to\mathbf{r}'}=\left[\infty+\frac{ik_0}{6\pi}\right]\overleftrightarrow{\mathbf{I}}. \tag{3.1.14}$$

the only term that is neither zero or infinite is the leading imaginary term [Vlack, 2012].

We can formally solved equation (3.1.6) using the classical Green's tensor to give

$$\hat{\mathbf{E}}(\mathbf{r},\omega) = i\mu_0\omega \int d^3r' \overleftrightarrow{\mathbf{G}}(\mathbf{r},\mathbf{r}';\omega)\cdot\hat{\mathbf{J}}_N(\mathbf{r}',\omega)\,. \tag{3.1.15}$$

From equations (3.1.4a), (3.1.4b) and (3.1.3a) in the Schrödinger picture of electric field operator, is written as

$$\hat{\mathbf{E}}(\mathbf{r}) = \int_0^\infty d\omega \sum_{\lambda=e,m}\int d^3r' \overleftrightarrow{\mathbf{G}}_\lambda(\mathbf{r},\mathbf{r}';\omega)\cdot\hat{\mathbf{f}}_\lambda(\mathbf{r}',\omega) + \text{H.C.} \tag{3.1.16}$$

where the expansion coefficients are given by [Buhmann, 2012]

$$\overleftrightarrow{\mathbf{G}}_e(\mathbf{r},\mathbf{r}';\omega) = ik_0^2\sqrt{\frac{\hbar}{\pi\epsilon_0}\text{Im}\left[\epsilon(\mathbf{r}',\omega)\right]}\overleftrightarrow{\mathbf{G}}(\mathbf{r},\mathbf{r}';\omega) \tag{3.1.17a}$$

$$\overleftrightarrow{\mathbf{G}}_m(\mathbf{r},\mathbf{r}';\omega) = ik_0\sqrt{\frac{\hbar}{\pi\epsilon_0}\frac{\text{Im}\left[\mu(\mathbf{r}',\omega)\right]}{|\mu(\mathbf{r}',\omega)|^2}}\left[\boldsymbol{\nabla}'\times\overleftrightarrow{\mathbf{G}}(\mathbf{r}',\mathbf{r};\omega)\right]^{\text{T}}. \tag{3.1.17b}$$

These tensors can be shown to obey the integral relation

$$\sum_{\lambda=e,m}\int d^3s\,\overleftrightarrow{\mathbf{G}}_\lambda(\mathbf{r},\mathbf{s};\omega)\cdot\overleftrightarrow{\mathbf{G}}_\lambda^{*\text{T}}(\mathbf{r}',\mathbf{s};\omega) = \frac{\hbar\mu_0}{\pi}\omega^2\text{Im}\left[\overleftrightarrow{\mathbf{G}}(\mathbf{r},\mathbf{r}',\omega)\right] \tag{3.1.18}$$

which follow directly from the integral relation of the Green's tensor

$$\int d^3s\left\{-\frac{\text{Im}\left[\mu(\mathbf{s},\omega)\right]}{|\mu(\mathbf{s},\omega)|^2}\left[\overleftrightarrow{\mathbf{G}}(\mathbf{r},\mathbf{s},\omega)\times\overleftarrow{\boldsymbol{\nabla}}_s\right]\cdot\left[\boldsymbol{\nabla}_s\times\overleftrightarrow{\mathbf{G}}^*(\mathbf{s},\mathbf{r}',\omega)\right]\right. \tag{3.1.19}$$

$$\left. + k_0^2\text{Im}\left[\epsilon(\mathbf{s},\omega)\right]\overleftrightarrow{\mathbf{G}}(\mathbf{r},\mathbf{s},\omega)\cdot\overleftrightarrow{\mathbf{G}}^*(\mathbf{s},\mathbf{r}',\omega)\right\} = \text{Im}\left[\overleftrightarrow{\mathbf{G}}(\mathbf{r},\mathbf{r}',\omega)\right]$$

as we show in Appendix B, and where

$$\left[\overleftrightarrow{\mathbf{G}}(\mathbf{r},\mathbf{s},\omega)\times\overleftarrow{\boldsymbol{\nabla}}_{\mathbf{s}}\right]_{ij} = \epsilon_{jkl}\partial_k^s G_{il}(\mathbf{r},\mathbf{s},\omega)\,. \tag{3.1.20}$$

All the relevant information about physical bodies such as their geometry or properties such as dispersion and absorption are contained in the Green's tensor. It is worth nothing that the Green's tensor can be computed analytically for a variety of simple configurations including planar geometries, spheres and cylinders.

The vacuum expectation value of the electric field (3.1.15) is obviously zero, whereas the fluctuation of the electric field is not. Using equations (3.1.5a) and (3.1.5b) together with (3.1.19) we obtain

$$\langle\{0\}|\,\hat{E}_n(\mathbf{r},\omega)\,\hat{E}_m(\mathbf{r}',\omega')\,|\{0\}\rangle = \frac{\hbar\omega^2}{\pi\epsilon_0 c^2}\text{Im}\left[G_{nm}(\mathbf{r},\mathbf{r}',\omega)\right]\delta(\omega-\omega') \tag{3.1.21}$$

where $|\{0\}\rangle$ is the ground state of the field. Equation (3.1.21) reveals that the fluctuation of the electromagnetic field is determined by the imaginary part of the Green's tensor, result that is consistent with the dissipation-fluctuation theorem. Thus, the quantization scheme respects the correct commutation relations and statistical physics.

3.2 Atom field interaction

Let us consider a neutral two level atom that resonantly interacts with radiation via an electric dipole transition. We model the total Hamiltonian as [Buhmann S. Y., 2008]

$$\hat{H} = \hat{H}_A + \hat{H}_F + \hat{H}_{AF} \tag{3.2.1}$$

where the first term describes the atom as

$$\hat{H}_A = \hbar\omega_{10} |1\rangle \langle 1| \tag{3.2.2}$$

with ω_{10} being the energy gap between the electronic excited state and the ground state. The field Hamiltonian is given by

$$\hat{H}_F = \sum_{\lambda} \int d^3r \int_0^{\infty} d\omega \hbar\omega \hat{\mathbf{f}}_{\lambda}^{\dagger}(\mathbf{r},\omega) \cdot \hat{\mathbf{f}}_{\lambda}(\mathbf{r},\omega). \tag{3.2.3}$$

In the atom field interaction, the multipolar hamiltonian describing the interaction of an atom with the field can be written as

$$\hat{H}_{AF} = -\hat{\mathbf{d}}_A \cdot \hat{\mathbf{E}}(\mathbf{r}_A) \tag{3.2.4}$$

where $\mathbf{r}_A$ is the position of the two level atom.

A two level atom with the field given by (3.1.16), the electric dipole model is defined as

$$\hat{\mathbf{d}}_A = \mathbf{d}_A^{01} \cdot \hat{\sigma}_A + \text{H.C.} \tag{3.2.5}$$

with $\mathbf{d}_A^{mn} = \langle m_A| \hat{\mathbf{d}}_A |n_A\rangle$, $\mathbf{d}_A^{mm} = 0$ and $\hat{\sigma}_A = |0\rangle \langle 1|$.

Using equation (3.1.16) together with (3.2.5), the interaction Hamiltonian becomes

$$\hat{H}_{AF} = -\sum_{\lambda=e,m} \int_0^{\infty} d\omega \int d^3r \left(\mathbf{d}_A^{01}\hat{\sigma}_A + \mathbf{d}_A^{10}\hat{\sigma}_A^{\dagger}\right) \left(\overleftrightarrow{\mathbf{G}}_{\lambda}(\mathbf{r}_A,\mathbf{r};\omega) \cdot \hat{\mathbf{f}}_{\lambda}(\mathbf{r},\omega) + H.C.\right). \tag{3.2.6}$$

For convenience, we introduce an additional set of position dependent creation and annihilation operators according to the definition

$$\hat{a}(\mathbf{r},\omega) = -\frac{1}{\hbar g(\mathbf{r},\omega)} \sum_{\lambda=e,m} \int d^3r' \mathbf{d}_A^{10} \cdot \overleftrightarrow{\mathbf{G}}_{\lambda}(\mathbf{r},\mathbf{r}';\omega) \cdot \hat{\mathbf{f}}_{\lambda}(\mathbf{r}',\omega) \tag{3.2.7}$$

where

$$g(\mathbf{r},\omega) = \sqrt{\frac{\mu_0}{\hbar\pi}\omega^2 \mathbf{d}_A^{10} \cdot \text{Im}\left[\overleftrightarrow{\mathbf{G}}(\mathbf{r},\mathbf{r};\omega)\right] \cdot \mathbf{d}_A^{01}} \tag{3.2.8}$$

is the atom-field coupling strength. Substitution of these into $\hat{H}_{AF}$ and invoking the rotating-wave approximation RWA, gives

$$\hat{H}_{AF} = \int_0^{\infty} d\omega \hbar g(\mathbf{r}_A,\omega) \left[\hat{a}(\mathbf{r}_A,\omega)\hat{\sigma}_A^{\dagger} + \hat{a}^{\dagger}(\mathbf{r}_A,\omega)\hat{\sigma}_A\right] \tag{3.2.9}$$

which shows that $g(\mathbf{r},\omega)$ may be regarded as a generalized atom-field coupling strength.

The commutation relations for $\hat{a}(\mathbf{r}_A,\omega)$ and $\hat{a}^\dagger(\mathbf{r}_A,\omega)$ can be found using the bosonic commutations equations (3.1.5a) and (3.1.5b), together with the definitions (3.2.7), (3.2.8) and the integral relation (3.1.18), resulting in (Appendix C)

$$\left[\hat{a}(\mathbf{r},\omega),\hat{a}^\dagger(\mathbf{r}',\omega')\right]=\frac{g(\mathbf{r},\mathbf{r}',\omega)}{g(\mathbf{r},\omega)\,g(\mathbf{r}',\omega)}\delta(\omega-\omega') \tag{3.2.10a}$$

$$\left[\hat{a}(\mathbf{r},\omega),\hat{a}(\mathbf{r},\omega')\right]=0 \tag{3.2.10b}$$

$$\left[\hat{a}(\mathbf{r},\omega),\hat{a}^\dagger(\mathbf{r},\omega')\right]=\delta(\omega-\omega'). \tag{3.2.10c}$$

where the function

$$g(\mathbf{r},\mathbf{r}',\omega)=\frac{\mu_0}{\hbar\pi}\omega^2\mathbf{d}_A^{10}\cdot\mathrm{Im}\left[\overleftrightarrow{\mathbf{G}}(\mathbf{r},\mathbf{r}';\omega)\right]\cdot\mathbf{d}_A^{01} \tag{3.2.11}$$

is the spectral density of the system, which characterizes the action of the absorbing medium on a two level atom with dipole moment $\hat{\mathbf{d}}_A$.

From the definition of the ground state $|\{0\}\rangle$ of the system composed of the background material and the electromagnetic field, $\hat{\mathbf{f}}_\lambda(\mathbf{r},\omega)|\{0\}\rangle=0\ (\forall\,\lambda,\mathbf{r},\omega)$, imply that

$$\hat{a}(\mathbf{r},\omega)|\{0\}\rangle=0.\qquad\forall\,\mathbf{r},\omega \tag{3.2.12}$$

The operator $\hat{a}^\dagger(\mathbf{r},\omega)$, can be used to define single excitation states

$$\hat{a}^\dagger(\mathbf{r},\omega)|\{0\}\rangle=|\{\mathbf{1}(\mathbf{r},\omega)\}\rangle \tag{3.2.13}$$

where $|\{\mathbf{1}(\mathbf{r},\omega)\}\rangle$ is a single photon continuum Fock state.

From equation (3.2.10a), we obtain

$$\langle\{\mathbf{1}(\mathbf{r},\omega)\}|\,\{\mathbf{1}(\mathbf{r}',\omega')\}\rangle=\frac{g(\mathbf{r},\mathbf{r}',\omega)}{g(\mathbf{r},\omega)\,g(\mathbf{r}',\omega)}\delta(\omega-\omega') \tag{3.2.14a}$$

$$\langle\{\mathbf{1}(\mathbf{r},\omega)\}|\,\{\mathbf{1}(\mathbf{r},\omega')\}\rangle=\delta(\omega-\omega') \tag{3.2.14b}$$

in others words, the states are orthogonal with respect to frequency ω but not position $\mathbf{r}$. This reflects the fact that there is a non-zero probability for the photons emitted by an atom positioned at $\mathbf{r}$ to be absorbed by an atom at a different position $\mathbf{r}'$.

Furthermore, the states $|\{\mathbf{1}(\mathbf{r},\omega)\}\rangle$ are eigenstates of $\hat{H}_F$ carrying one quantum of energy, i.e,

$$\hat{H}_F|\{\mathbf{1}(\mathbf{r},\omega)\}\rangle=\hbar\omega|\{\mathbf{1}(\mathbf{r},\omega)\}\rangle. \tag{3.2.15}$$

3.3 Quantum dynamics of an excited atom

In order to explore the quantum dynamics of an atomic emitter, we start from the time dependent Schrödinger equation $i\hbar\partial|\psi(t)\rangle/\partial t=\hat{H}|\psi(t)\rangle$ and use a wavefunction ansatz based on the Wigner-Weisskopf theory. In this ansatz, the time dependent state $|\psi(t)\rangle$ of the system can be expanded

by a complete set of state vectors formed by electronic and polariton states [Vogel W., 2006]

$$|\psi(t)\rangle = C_{1\{0\}}(t)\, e^{-i\omega_{10}t}\,|1\rangle\,|\{0\}\rangle + \int_0^\infty d\omega C_{0\{1\}}(\mathbf{r}_A,\omega,t)\, e^{-i\omega t}\,|0\rangle\,|\{\mathbf{1}(\mathbf{r}_A,\omega)\}\rangle \tag{3.3.1}$$

where $C_{1\{0\}}(t)$ and $C_{0\{1\}}(\mathbf{r}_A,\omega,t)$ are the coefficients of the electronic excited state (subscript 1) with zero photon state (subscript $\{0\}$) and the electronic ground state (subscript 0) with one photon state having a certain polarization (subscript $\{1\}$).

Substituting equation (3.3.1) into the Schrödinger equation and after some algebra see Appendix D, one can derive a set of differential equations for the state amplitudes that need

$$i\hbar\dot{C}_{1\{0\}}(t)\, e^{-i\omega_{10}t} = \int_0^\infty d\omega\hbar g(\mathbf{r}_A,\omega)\, C_{0\{1\}}(\mathbf{r}_A,\omega,t)\, e^{-i\omega t} \tag{3.3.2a}$$

$$i\hbar\dot{C}_{0\{1\}}(t)\, e^{-i\omega t} = \hbar g(\mathbf{r}_A,\omega)\, e^{-i\omega_{10}t} C_{1\{0\}}(t)\,. \tag{3.3.2b}$$

To solve these under the initial condition $C_{1\{0\}}(t=0) = C_{1\{0\}}(0)$ and $C_{0\{1\}}(\mathbf{r}_A,\omega,t=0) = C_{0\{1\}}(\mathbf{r}_A,\omega,0)$, we formally integrate the equation (3.3.2b) and insert the result in the equation (3.3.2a). After some algebra we derive the integro-differential equation

$$\dot{C}_{1\{0\}}(t) = -\int_0^t dt' K(t-t')\, C_{1\{0\}}(t') + f(t) \tag{3.3.3}$$

where the kernel function is given by

$$K(t-t') = \int_0^\infty d\omega \frac{\mu_0}{\hbar\pi}\omega^2 \mathbf{d}_A^{10}\cdot \mathrm{Im}\left[\overleftrightarrow{\mathbf{G}}(\mathbf{r}_\mathrm{A},\mathbf{r}_\mathrm{A};\omega)\right]\cdot\mathbf{d}_A^{01} e^{-i\left(t-t'\right)(\omega-\omega_{10})} \tag{3.3.4}$$

and the source term by

$$f(t) = -i\int_0^\infty d\omega \sqrt{\frac{\mu_0}{\hbar\pi}\omega^2 \mathbf{d}_A^{10}\cdot \mathrm{Im}\left[\overleftrightarrow{\mathbf{G}}(\mathbf{r}_\mathrm{A},\mathbf{r}_\mathrm{A};\omega)\right]\cdot\mathbf{d}_A^{01}}\, e^{-i(\omega-\omega_{10})t} C_{0\{1\}}(\mathbf{r}_A,\omega,0) \tag{3.3.5}$$

Equation (3.3.3) is a system of Volterra type integro-differential equation, including non Markovian effects and it can be solved numerically. The evolution equation is general for a two level atom in presence of inhomogeneous, dispersive and absorbing media.

We can follow the same procedure to get the equation for the photon amplitude, obtaining

$$\dot{C}_{0\{1\}}(\mathbf{r}_A,\omega,t) = -d(t)\int_0^t dt' k(t-t')\, C_{0\{1\}}(\mathbf{r}_A,\omega,t') + h(t) \tag{3.3.6}$$

where the kernel function is given by

$$k(t-t') = \int_0^\infty d\omega \sqrt{\frac{\mu_0}{\hbar\pi}\omega^2 \mathbf{d}_A^{10}\cdot \mathrm{Im}\left[\overleftrightarrow{\mathbf{G}}(\mathbf{r}_\mathrm{A},\mathbf{r}_\mathrm{A};\omega)\right]\cdot\mathbf{d}_A^{01}}\, e^{-i(\omega-\omega_{10})t'} \tag{3.3.7}$$

$$d(t) = \sqrt{\frac{\mu_0}{\hbar\pi}\omega^2 \mathbf{d}_A^{10}\cdot \mathrm{Im}\left[\overleftrightarrow{\mathbf{G}}(\mathbf{r}_\mathrm{A},\mathbf{r}_\mathrm{A};\omega)\right]\cdot\mathbf{d}_A^{01}}\, e^{i(\omega-\omega_{10})t} \tag{3.3.8}$$

and

$$h\left(t\right)=-i\sqrt{\frac{\mu_0}{\hbar\pi}\omega^2\mathbf{d}_A^{10}\cdot\mathrm{Im}\left[\overleftrightarrow{\mathbf{G}}\left(\mathbf{r}_\mathrm{A},\mathbf{r}_\mathrm{A};\omega\right)\right]\cdot\mathbf{d}_A^{01}}e^{i(\omega-\omega_{10})t}C_{1\{0\}}\left(0\right). \tag{3.3.9}$$

All of the material parameters relevant for the atomic evolution are contained in the kernel functions via the Green's tensor of the system, which we can obtain numerically using the FDTD method.

Chapter 4

Quantum dynamics of a single atom near a Drude nanoantenna

As we discuss in Chapter 1, metal-dielectric interfaces strongly modify the density of electromagnetic modes of their surrounding. This is due to the existence of surface modes, known as surface plasmon polaritons (SPP), which propagate along the metal surface.

A two level atom in a metal dielectric interface can be considered as an open quantum system that is strongly coupled to a reservoir, given by the plasmon field. The system exhibits a complex dynamics, beyond simple Markovian evolutions.

Nowadays, it is possible to make nanoantennas whose nanogaps are sub 5 [nm] Figure (4.1.1). Such nanogaps localizing the electromagnetic waves that exceeds the diffraction limit and confine the radiation, are used to probe optical properties in single-molecules Raman scattering to obtain large enhancement factors or even to control a variety of photochemical reactions systems using the excitation of plasmon resonance [Ueno K., 2013].

In this Thesis, we study dynamics of a two level atom in different plasmonic environment, where we use the Green's tensor approach to obtain the spectral densities of these systems and study the quantum dynamics of the excited state of an emitter with two levels that can be an atom or molecule.

4.1 Quantum dynamics of a two level system over a infinite - Drude metal plane

We study the quantum dynamics of a two level atom close to a planar Drude infinite surface as shown in Figure (4.1.2), which supports a surface plasmon field. The atom is located at different heights z. As discussed in Chapter 2, in order to simulate infinite length structures in FDTD, these must penetrate the Absorbing Boundary Condition in the computational space.

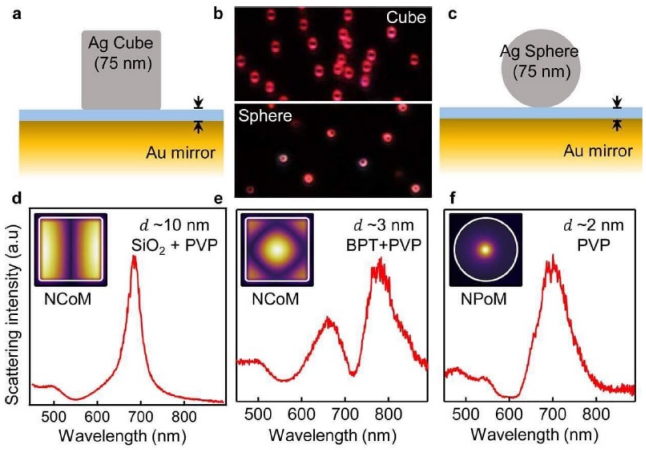

Figure 4.1.1: Comparison between nanocubes and nanospheres over a gold mirror. (a) Schematic of a silver nanocube with 75 [nm] edge length over a gold mirror with sub 5 [nm] molecular gaps. (b) Optical dark-field images of (top) nanocubes and (bottom) nanospheres placed on a gold mirror with BPT and PVP spacers, respectively. (d-f) Schematic NPoM. Scattering spectra from 75 [nm] nanocubes with (d) 10 [nm] SiO2 spacer and (e) 3 [nm] BPT spacer and (f) nanosphere with 2 [nm] PVP spacer. Ref.[Chikkaraddy et al., 2017].

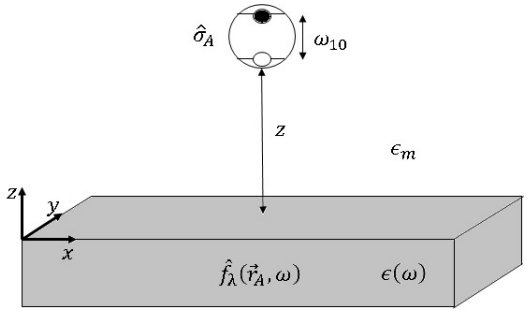

Figure 4.1.2: A two level atom emitter with Pauli operator $\hat{\sigma}_A$, and frequency ω_{10} is at a distance z above a infinity planar metal surface (silver) with $\hat{\mathbf{f}}_\lambda(\mathbf{r},\omega)$ the bosonic field in the medium modeled using a Drude model $\epsilon(\omega)$ and ϵ_m is the dielectric medium.

As a first step for computing the dynamics of the two level atom, we compute the spectral density $g(\mathbf{r},\mathbf{r}',\omega)$ that determines the evolution kernel $K(t-t')$ equation (3.3.4) introduced in Chapter 3. We do this for two different sets of Drude parameters, we made two simulations for a two level atom above a metal planar surface, and we obtain two different plasmon resonances for the spectral density of the system. The first Drude parameter set is $\omega_p = 8.9$ [eV], $\gamma_p = 0.24$ [eV] and $\epsilon_\infty = 7$, as reported in Ref.[Yang et al., 2015]. The second set is $\omega_p = 3.76$ [eV], $\gamma_p = 0.1128$ [eV] and $\epsilon_\infty = 9.6$, reported in Ref.[Gonzalez-Tudela et al., 2010]. The same resonance frequency of the two level atom $\omega_{10} = 480$ [THz] used for both simulations. The plasmon resonance frequency for this planar geometry occurs at $\omega_{sp} = {\omega_p}/{\sqrt{\epsilon_m+\epsilon_r}}$ [Maier, 2007]. For the first set of parameters the plasmon resonance is at $\omega_{sp} = 2.6$ [eV] and the second case at $\omega_{sp} = 0.9$ [eV]. The results in Figure (4.1.3) show that the choice of Drude parameters is very important to obtain good quantitative results.

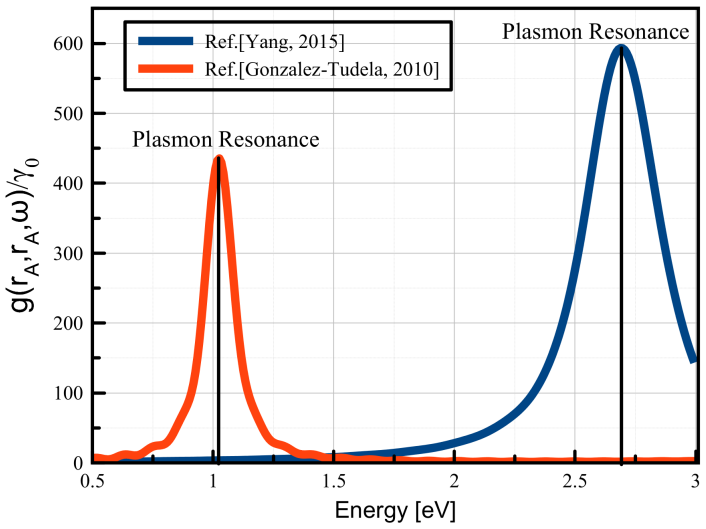

Figure 4.1.3: Spectral density normalized by the spontaneous emission rate in free space γ_0. Two simulations for two different Drude parameters, where we used $\omega_p = 8.9$ [eV], $\gamma_p = 0.24$ [eV] and $\epsilon_\infty = 7$, reported in Ref.[Gonzalez-Tudela et al., 2010] (blue line) and $\omega_p = 3.76$ [eV], $\gamma_p = 0.1128$ [eV] and $\epsilon_\infty = 9.6$, reported in Ref.[Yang et al., 2015] (red line), with $\omega_{10} = 480$ [THz].

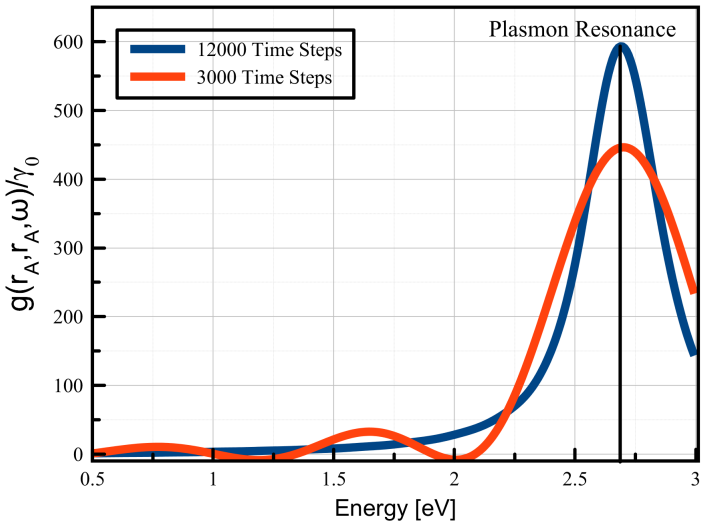

Figure 4.1.4: Spectral density normalized by the spontaneous emission rate in free space γ_0 for two different simulation using 12000 time steps and 3000 time steps in FDTD for a two level atom with $\omega_{10} = 480$ [THz] at $z = 5$ [nm] and Drude parameters $\omega_p = 8.9$ [eV], $\gamma_p = 0.24$ [eV] and $\epsilon_\infty = 7$.

In order to compute an accurate spectral density at the location of the atom $g(\mathbf{r}_A, \mathbf{r}_A, \omega)$, the total integration time of the FDTD simulation is important. In order to show this, we made two

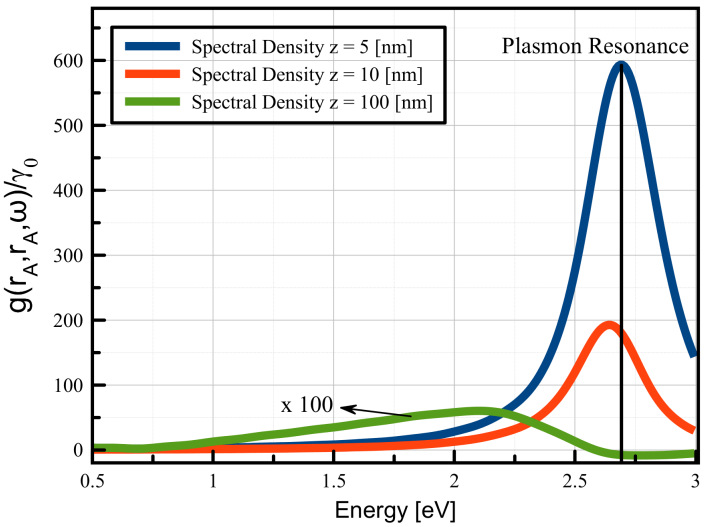

Figure 4.1.5: Spectral density normalized by the spontaneous emission rate in free space γ_0 for a two level atom with $\omega_{10} = 480$ [THz] at different heights $z = 5,\ 10$ and 100 [nm] and using Drude parameters reported in Ref.[Yang et al., 2015]. Green line was multiplied by 100.

simulations. For a two level atom above a Drude metal at $z = 5$ [nm] with 3000 time steps and 12000 time steps. We use the Drude parameters in Ref.[Yang et al., 2015] with the resonance frequency of the two level atom $\omega_{10} = 480$ [THz]. For a smaller integration time, the lower frequency part of the spectral density develops artificial oscillations. These disappear by increasing the total integration time, while keeping the main peak invariant.

The spectral density also depends on the location of the atom above the metal surface $\mathbf{r}_A$. In Figure (4.1.5), we plot $g\left(\mathbf{r}_A, \mathbf{r}_A, \omega\right)$ for different heights of the two level atom from the surface $z = 5,\ 10$ and 100 [nm]. The spectral density is normalized by the spontaneous decay rate in free space γ_0. We can see a reduction in the spectral density when the two level system gets further away from the surface. For small separations, the strong peak occurs at the plasmon resonance. For large separations, the peak broadens and shifts to longer wavelengths. These results are consistent with the study in Ref.[Gonzalez-Tudela et al., 2010].

In order to obtain the evolution kernel of the system $K\left(t - t'\right)$, we solve the one-sided Fourier transform in Equation (3.3.4) for the spectral density. We do this for 3000 time steps and 12000 FDTD time steps, in order to see the effect of the FDTD integration time in the quantum dynamics of the atom.

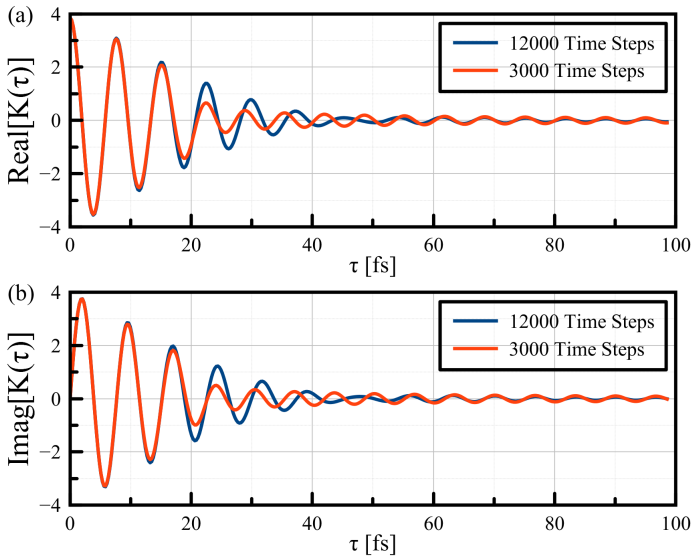

Figure 4.1.6: Real (a) and imaginary (b) part of kernel at $z = 5$ [nm] of a two level atom with $\omega_{10} = 480$ [THz] and using Drude parameters reported in Ref.[Yang et al., 2015], for 12000 Time Steps and 3000 Time Steps in FDTD.

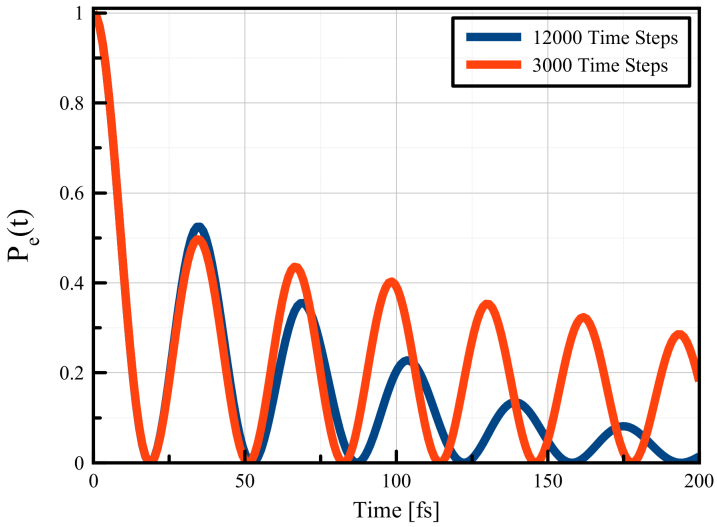

Figure 4.1.7: Excited state population dynamics for two simulations at $z = 5$ [nm] from the silver surface using the Drude parameters reported in Ref.[Yang et al., 2015], with a characteristic frequency $\omega_{10} = 480$ [THz]. Kernel obtained with 12000 time steps and with 3000 time steps in FDTD. The population dynamics decay slower for spectral densities that have artificial components at low frequencies.

After constructing the kernel $K\left(t - t'\right)$, we solve the non-Markovian evolution equation for the quantum dynamics for the two level atom Equation (3.3.3), using a home-built using an integro-

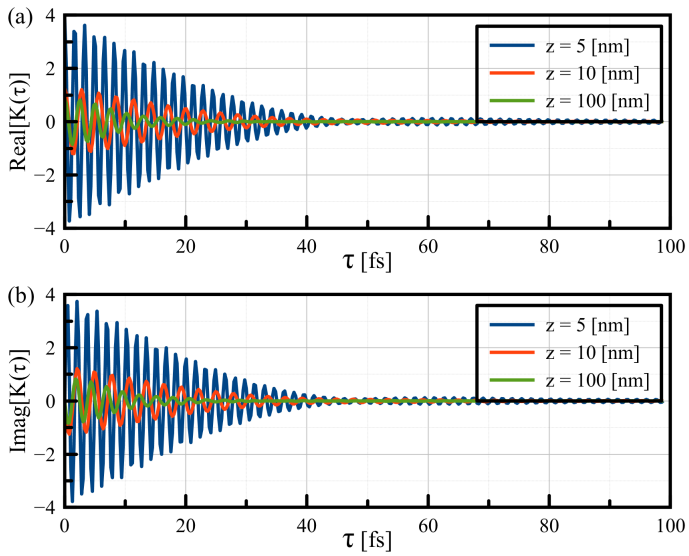

Figure 4.1.8: Real (a) and imaginary (b) part of kernels for different heights at $z = 5$ [nm] (blue line), 10 [nm] (red line) and 100 [nm] (green line), where the green line was increased by a factor 10^2.

differential equation (IDE) solver in MATLAB, following the same algorithm in Ref.[Gelmi C. A., 2014]. This method uses a relaxation parameter in the context of iterative methods for linear systems capable of solving a wide variety of IDE of arbitrary order, including the Volterra and Fredholm IDE with variable limits on the integral and non-linear IDE. The solver performs successive relaxation iterations until convergence is achieved.

To specify the initial condition for the wave function Equation (3.3.1), the two level atom is set to be in its excited state $\left(C_{1\{0\}}\left(0\right)=1\right)$ which decays by emitting a near field photon with $\left(C_{0\{1\}}\left(\mathbf{r}_A,\omega,0\right)=0 \text{ and } f\left(t\right)=0\right)$. The two level atom has a characteristic frequency $\omega_{10}=480$ [THz]. Figure (4.1.7) shown the resulting Rabi oscillations of the population dynamics for an atom at 5 [nm] from the surface. The figure also shows that the computed qubit decay dynamics is very sensitive to the quality of the spectral density. This behavior is due to the artificial low frequency oscillations in spectral density of the system that are present for short FDTD integration times.

For 12000 time steps in FDTD and using the same Drude parameters as in Figure (4.1.7), we plot the kernels for different atom-surface distance $z = 5$, 10 and 100 [nm]. The amplitude and the oscillations frequency of the kernels increase as the distance decreases.

Using the IDE method implemented following in Ref.[Gelmi C. A., 2014], we solve the evolution equation (3.3.3), with $\left(C_{1\{0\}}\left(0\right)=1\right)$, without initial photons $\left(C_{0\{1\}}\left(\mathbf{r}_A,\omega,0\right)=0 \text{ and } f\left(t\right)=0\right)$ for an atom frequency $\omega_{10}=480$ [THz], and different heights. We can see how the Rabi oscillations are not present when the atom is localized at distances far enough from the metal Drude plane. The oscillations are present when the atom-surface distance is small.

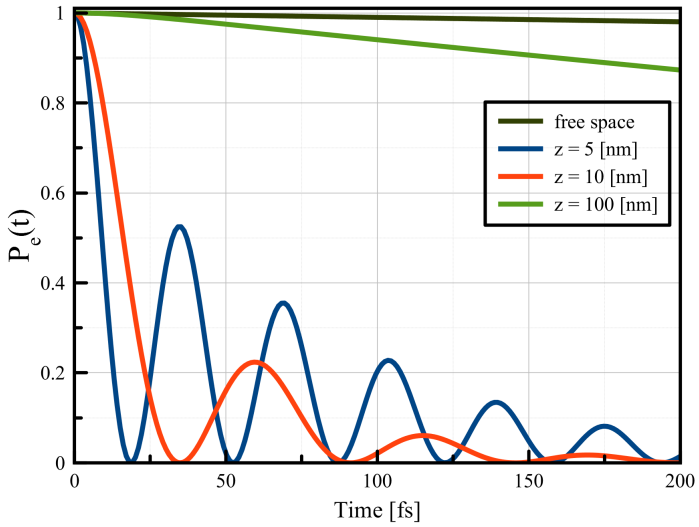

Figure 4.1.9: Excited state population $P_e\,(t)$ for a two level atom over a Drude surface at different heights $z = 5$ [nm] (blue line), 10 [nm] (red line) and 100 [nm] (green line), with frequency $\omega_{10} = 480$ [THz].

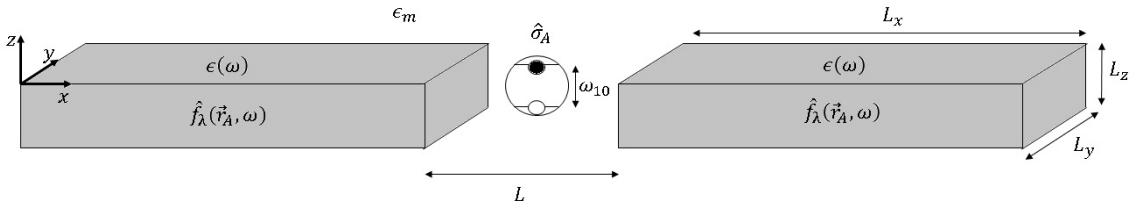

Figure 4.1.10: A two level atomic emitter with Pauli operators $\hat{\sigma}_A$ and frequency ω_{10} is at the gap L between a two planar metal surface (silver) with $\hat{\mathbf{f}}_\lambda\,(\mathbf{r},\omega)$, being the bosonic field of the metal modeled using a Drude model $\epsilon\,(\omega)$ and ϵ_m is the dielectric medium.

4.2 Quantum dynamics of a two level atom in a Drude metal nanoantenna

We study the quantum dynamics of a two level atom in a Drude metal gap nanoantenna with dimensions $L_x = 60$ [nm], $L_y = 20$ [nm] and $L_z = 10$ [nm] as we can see in Figure (4.1.10). We do this for two polarizations of the two level atom along $\hat{\mathbf{x}}$ and $\hat{\mathbf{z}}$ directions.

Using 30000 time steps with the Drude model parameters reported in [Yang et al., 2015], we made two simulations for a the gap distances $L = 5$ and 10 [nm] where the two level atom is at the center of the nanoantenna, with $\omega_{10} = 480$ [THz]. We can see that two peaks appears in the spectral density of this system, which is the result of the coupling of the plasmon modes of each rectangular arm of the nanoantenna.

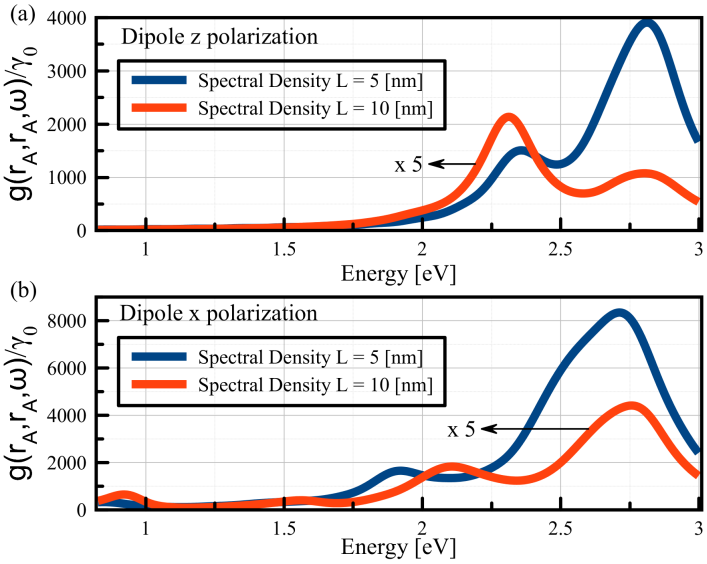

Figure 4.2.1: Spectral density of a two level atom between two metal Drude bricks normalized by the spontaneous emission in free space γ_0 and $\omega_{10} = 480$ [THz] with (a) $\hat{\mathbf{z}}$ polarization and (b) $\hat{\mathbf{x}}$ polarization at different separation distances $L = 5$ and 10 [nm] and using Drude parameters reported in Ref.[Yang et al., 2015]. Red line was multiplied by 5.

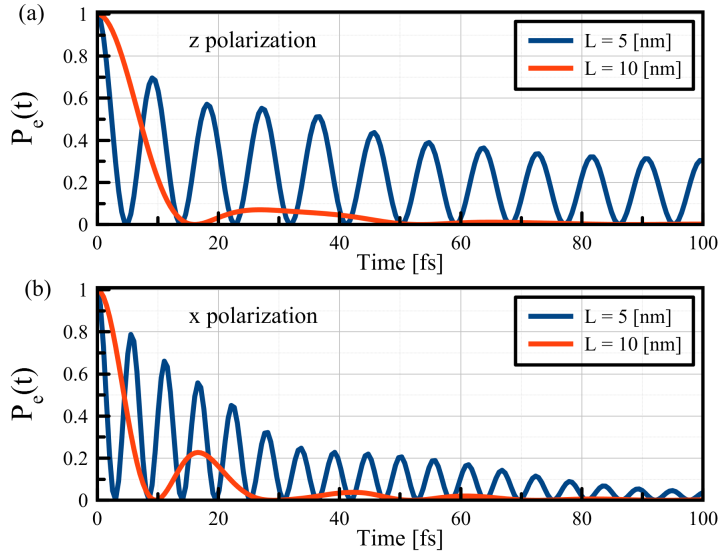

Figure 4.2.2: Excited population dynamics $P_e(t)$ of a two level atom with a characteristic frequency $\omega_{10} = 480$ [THz] in the gap of a Drude metal nanoantenna, with two different gaps $L = 5$ and 10 [nm] for (a) $\hat{\mathbf{z}}$ polarization and (b) $\hat{\mathbf{x}}$ polarization.

We compute the population dynamics of the atom with a transition dipole polarization along $\hat{\mathbf{x}}$ and $\hat{\mathbf{z}}$ directions, using the IDE method in Ref.[Gelmi C. A., 2014]. We considered the two level

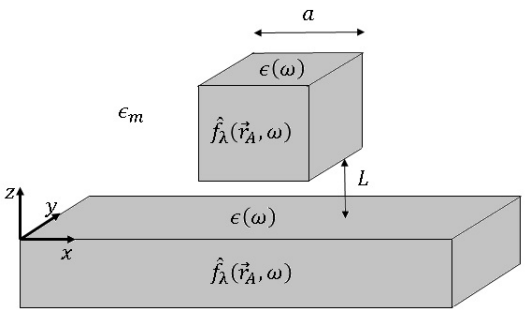

Figure 4.2.3: NPoM geometry using a Drude model $\epsilon(\omega)$, where $\hat{\mathbf{f}}_\lambda(\mathbf{r},\omega)$ is the bosonic field and ϵ_m is the dielectric medium. The emitter is in the gap, where the gap distance is $L = 5$ [nm].

system is to be initially preparated in its excited state $\left(C_{1\{0\}}(0) = 1\right)$, without photons in the field $\left(C_{0\{1\}}(\mathbf{r}_A,\omega,0) = 0 \text{ and } f(t) = 0\right)$ and with a two level atom with characteristic frequency $\omega_{10} = 480$ [THz]. We can observe decaying Rabi oscillations similar to the case of the atomic dipole with a separation of $z = 10$ [nm] from an infinite Drude plane. However, a gap lenght $L = 5$ [nm] the Rabi oscillations decay over longer timescales, that is the result of the strong coupling of the emitter with plasmons in the gap.

4.3 Quantum dynamics of a two level atom in a NPoM geometry

We finally study the quantum dynamics of a two level atom in the gap of a NPoM geometry, for a gap separation of 5 [nm], as we show in Figure (4.2.3). The nanocube has an edge length $a = 20$ [nm].

Using 30000 time steps in FDTD with the Drude model parameters reported in Ref.[Yang et al., 2015], we made two simulation, for $\hat{\mathbf{z}}$ and $\hat{\mathbf{x}}$ polarization of the emitting light by the two level atom, where $\omega_{10} = 480$ [THz]. We can see that, for $\hat{\mathbf{x}}$ polarization, the spectral density only has a one peak, this peak is the plasmon resonance of the cavity while with a $\hat{\mathbf{z}}$ polarization, the spectral density has two peaks that correspond to the coupling of plasmon in the gap.

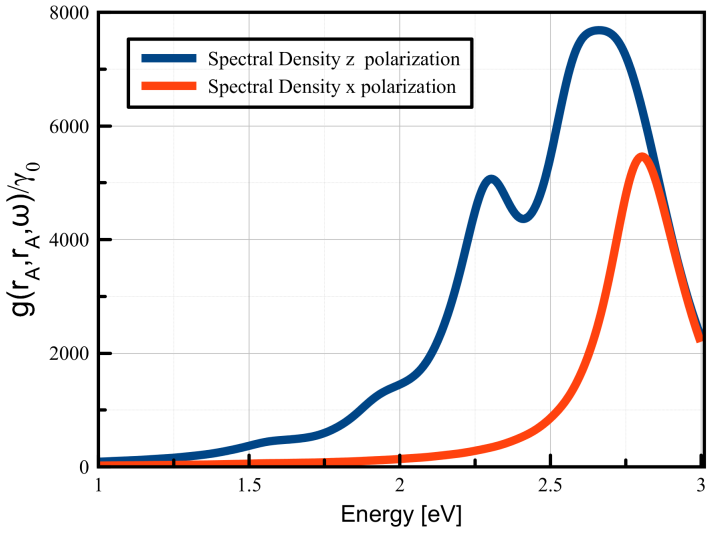

Figure 4.3.1: Spectral Density of a NPoM geometry normalized by the spontaneous emission rate in free space γ_0, with $\hat{\mathbf{z}}$ polarization (blue line) and $\hat{\mathbf{x}}$ polarization (red line).

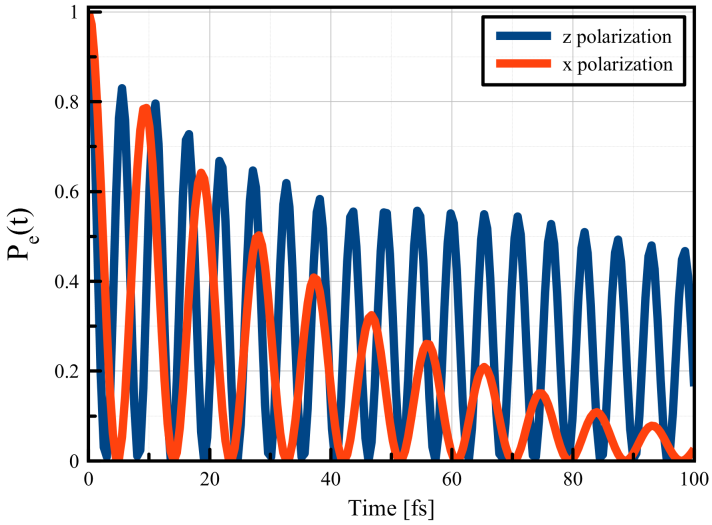

Figure 4.3.2: Excited population dynamics $P_e(t)$ of a two level atom between two Drude-metal NPoM geometry, with a gap separation of 5 [nm], where the coefficients are given by $C_{1\{0\}}(0) = 1$ and $C_{0\{1\}}(\mathbf{r}_A, \omega, 0) = 0$ with a characteristic frequency $\omega_{10} = 480$ [THz].

We obtain the population dynamics of this system, for both polarization direction $\hat{\mathbf{x}}$ and $\hat{\mathbf{z}}$. Using the IDE method in Ref.[Gelmi C. A., 2014] and considering that the two level system is prepared in its excited state $\left(C_{1\{0\}}(0) = 1\right)$, without polaritons $\left(C_{0\{1\}}(\mathbf{r}_A, \omega, 0) = 0 \text{ and } f(t) = 0\right)$. We can see that the strong coupling is achieved with both polarizations, $\hat{\mathbf{x}}$ and with $\hat{\mathbf{z}}$ polarization the Rabi oscillations decay over long timescales.

Conclusions and Outlook

In this Thesis, we have developed a macroscopic cavity QED treatment for light-matter interaction of single emitter in dispersive materials. Specifically, we use the Finite Difference Time Domain method (FDTD) to obtain the Green's tensor of a dipole source near a Drude material of arbitrary geometry, not limited to plasmonic materials. By considering the emitter as a two-level atom, we obtain the spectral density of the system (3.2.11), which describes the light-matter interaction strength as a function of position and frequency. The spectral density is determined by the classical Green's tensor of the problem. The evolution of the two-level atom is described by an integro-differential equation (3.3.3) with a memory kernel determined by this spectral density. We solve this IDE to obtain the population dynamics of the atom in its plasmonic environment.

The influence of the plasmonic modes provided by the conducting nanostructures, make them exceptional enhancers of single emitter light-matter interaction. It is possible to achieve strong coupling between single emitters like atoms or molecules with the electromagnetic environment of the nanostructures considered. By varying some control parameters such as the emitter-interface distance or the cavity length separation.

For an infinite Drude.metal system, the quantum dynamics of a two-level atom depends of the emitter-surface distance. Strong coupling is achieved at distance smaller than 10 [nm], as seen in the emergence of Rabi oscillations in the population dynamics. For a dipole nanoantenna with an emitter in the gap, it is possible to obtain strong coupling for an atomic dipole oriented parallel or orthogonal to the gap axis. The population decays over longer timescales, while for larger gaps, the population dynamics resembles that of the infinite plane. Finally, for a NPoM geometry it is possible to achieve strong coupling over longer timescales for both dipole orientations considered and the Rabi oscillations decay slowly.

As an outlook, this work can be extended to study the population dynamics of an emitter with molecular vibrations to study chemical reactions and how the rates of these reactions change with the geometry of the cavity used. Experiments in this direction can also motivate the development of theoretical tools and protocols for cavity-controlled chemistry in infrared cavities, strong coupling to vibrational transitions, in gas-phase molecules into infrared cavities should also be considered [Herrera F., 2020], and since the FDTD method is scalable, our work can be useful to study this type of realistic systems.

Bibliography

[Ammann, 2007] Ammann, M. W. (2007). *Non-Trivial Materials in EM-FDTD*. PhD thesis.

[Atkins et al., 2012] Atkins, P. R., Chew, W. C., Dai, Q. I., and Sha, W. E. I. (2012). The casimir force for arbitrary three-dimensional objects with low frequency methods. In *Proceedings of the 2012 IEEE International Symposium on Antennas and Propagation*. IEEE.

[Atwater H. A., 2010] Atwater H. A., P. A. (2010). Plasmonics for improved photovoltaic devices. *Nature Materials*, 9(3):205–213.

[Beggs et al., 1992] Beggs, J., Luebbers, R., Yee, K., and Kunz, K. (1992). Finite-difference time-domain implementation of surface impedance boundary conditions. *IEEE Transactions on Antennas and Propagation*, 40(1):49–56.

[Berenger, 2007] Berenger, J.-P. (2007). Perfectly matched layer (pml) for computational electromagnetics. *Synthesis Lectures on Computational Electromagnetics*, 2(1):1–117.

[Berens et al., 2016] Berens, M. K., Flintoft, I. D., and Dawson, J. F. (2016). Structured mesh generation: Open-source automatic nonuniform mesh generation for FDTD simulation. *IEEE Antennas and Propagation Magazine*, 58(3):45–55.

[Buechler et al., 1995] Buechler, D., Roper, D., Durney, C., and Christensen, D. (1995). Modeling sources in the FDTD formulation and their use in quantifying source and boundary condition errors. *IEEE Transactions on Microwave Theory and Techniques*, 43(4):810–814.

[Buhmann, 2012] Buhmann, S. Y. (2012). *Dispersion Forces I*. Springer Berlin Heidelberg.

[Buhmann S. Y., 2008] Buhmann S. Y., W. D. G. (2008). Casimir-polder forces on excited atoms in the strong atom-field coupling regime. *Physical Review A*, 77(1).

[Callahan et al., 2012] Callahan, D. M., Munday, J. N., and Atwater, H. A. (2012). Solar cell light trapping beyond the ray optic limit. *Nano Letters*, 12(1):214–218.

[Carnegie et al., 2018] Carnegie, C., Griffiths, J., de Nijs, B., Readman, C., Chikkaraddy, R., Deacon, W. M., Zhang, Y., Szabo, I., Rosta, E., Aizpurua, J., and Baumberg, J. J. (2018). Room-temperature optical picocavities below 1 nm3 accessing single-atom geometries. *The Journal of Physical Chemistry Letters*, 9(24):7146–7151.

[Cartar, 2017] Cartar, W. K. (2017). Theory and modelling of light-matter interactions in photonic crystal cavity systems coupled to quantum dot ensembles.

[Chikkaraddy et al., 2016] Chikkaraddy, R., de Nijs, B., Benz, F., Barrow, S. J., Scherman, O. A., Rosta, E., Demetriadou, A., Fox, P., Hess, O., and Baumberg, J. J. (2016). Single-molecule strong coupling at room temperature in plasmonic nanocavities. *Nature*, 535(7610):127–130.

[Chikkaraddy et al., 2017] Chikkaraddy, R., Zheng, X., Benz, F., Brooks, L. J., de Nijs, B., Carnegie, C., Kleemann, M.-E., Mertens, J., Bowman, R. W., Vandenbosch, G. A. E., Moshchalkov, V. V., and Baumberg, J. J. (2017). How ultranarrow gap symmetries control plasmonic nanocavity modes: From cubes to spheres in the nanoparticle-on-mirror. *ACS Photonics*, 4(3):469–475.

[Costen F., 2009] Costen F., J.-P. Berenger, A. B. (2009). Comparison of fdtd hard source with fdtd soft source and accuracy assessment in debye media. *IEEE Transactions on Antennas and Propagation*, 57(7):2014–2022.

[Dissanayake et al., 2010] Dissanayake, C. M., Premaratne, M., Rukhlenko, I. D., and Agrawal, G. P. (2010). FDTD modeling of anisotropic nonlinear optical phenomena in silicon waveguides. *Optics Express*, 18(20):21427.

[Dou L., 2006] Dou L., S. A. R. (2006). 3d fdtd method for arbitrary anisotropic materials. *Microwave and Optical Technology Letters*, 48(10):2083–2090.

[Gelmi C. A., 2014] Gelmi C. A., J. H. (2014). IDSOLVER: A general purpose solver for th-order integro-differential equations. *Computer Physics Communications*, 185(1):392–397.

[Giannini et al., 2011] Giannini, V., Fernandez-Dominguez, A. I., Heck, S. C., and Maier, S. A. (2011). Plasmonic nanoantennas: Fundamentals and their use in controlling the radiative properties of nanoemitters. *Chemical Reviews*, 111(6):3888–3912.

[Gonzalez-Tudela et al., 2010] Gonzalez-Tudela, A., Rodriguez, F. J., Quiroga, L., and Tejedor, C. (2010). Dissipative dynamics of a solid-state qubit coupled to surface plasmons: From non-markov to markov regimes. *Physical Review B*, 82(11).

[Herrera F., 2020] Herrera F., O. J. (2020). Molecular polaritons for controlling chemistry with quantum optics. *The Journal of Chemical Physics*, 152(10):100902.

[Herrera F., 2016] Herrera F., S. F. (2016). Cavity-controlled chemistry in molecular ensembles. *Physical Review Letters*, 116(23).

[Herrera F., 2017] Herrera F., S. F. (2017). Theory of nanoscale organic cavities: The essential role of vibration-photon dressed states. *ACS Photonics*, 5(1):65–79.

[Hopfield, 1958] Hopfield, J. J. (1958). Theory of the contribution of excitons to the complex dielectric constant of crystals. *Physical Review*, 112(5):1555–1567.

[Huang et al., 2009] Huang, X., Neretina, S., and El-Sayed, M. A. (2009). Gold nanorods: From synthesis and properties to biological and biomedical applications. *Advanced Materials*, 21(48):4880–4910.

[Hugall et al., 2018] Hugall, J. T., Singh, A., and van Hulst, N. F. (2018). Plasmonic cavity coupling. *ACS Photonics*, 5(1):43–53.

[Hutchison et al., 2012] Hutchison, J. A., Schwartz, T., Genet, C., Devaux, E., and Ebbesen, T. W. (2012). Modifying chemical landscapes by coupling to vacuum fields. *Angewandte Chemie International Edition*, 51(7):1592–1596.

[Huttner B., 1992] Huttner B., S. M. B. (1992). Dispersion and loss in a hopfield dielectric. *Europhysics Letters (EPL)*, 18(6):487–492.

[Jackson, 1998] Jackson, J. D. (1998). *Classical Electrodynamics*. John Wiley and Sons, Inc.

[Jones et al., 2018] Jones, R., Needham, J. A., Lesanovsky, I., Intravaia, F., and Olmos, B. (2018). Modified dipole-dipole interaction and dissipation in an atomic ensemble near surfaces. *Physical Review A*, 97(5).

[Joulain et al., 2003] Joulain, K., Carminati, R., Mulet, J.-P., and Greffet, J.-J. (2003). Definition and measurement of the local density of electromagnetic states close to an interface. *Physical Review B*, 68(24).

[Karanikolas, 2016] Karanikolas, V. D. (2016). *Interactions Between Quantum Emitters in the Presence of Plasmonic Nanostructures*. PhD thesis.

[Kauranen M., 2012] Kauranen M., Z. A. V. (2012). Nonlinear plasmonics. *Nature Photonics*, 6(11):737–748.

[Kelley D. F., 1996] Kelley D. F., L. R. J. (1996). Piecewise linear recursive convolution for dispersive media using FDTD. *IEEE Transactions on Antennas and Propagation*, 44(6):792–797.

[Knoll et al., 2000] Knoll, L., Scheel, S., and Welsch, D.-G. (2000). Qed in dispersing and absorbing media.

[Kongsuwan et al., 2017] Kongsuwan, N., Demetriadou, A., Chikkaraddy, R., Benz, F., Turek, V. A., Keyser, U. F., Baumberg, J. J., and Hess, O. (2017). Suppressed quenching and strong-coupling of purcell-enhanced single-molecule emission in plasmonic nanocavities. *ACS Photonics*, 5(1):186–191.

[Kunz, 1993] Kunz, Karl S.; Luebbers, R. J. (1993). *The Finite Difference Time Domain Method for Electromagnetics*. CRC Press, 1 edition.

[Kuzuoglu M., 1996] Kuzuoglu M., M. R. (1996). Frequency dependence of the constitutive parameters of causal perfectly matched anisotropic absorbers. *IEEE Microwave and Guided Wave Letters*, 6(12):447–449.

[Lal et al., 2008] Lal, S., Clare, S. E., and Halas, N. J. (2008). Nanoshell-enabled photothermal cancer therapy: Impending clinical impact. *Accounts of Chemical Research*, 41(12):1842–1851.

[Li et al., 2001] Li, L.-W., Kang, X.-K., Leong, M.-S., Kooi, P.-S., and Yeo, T.-S. (2001). Electromagnetic dyadic greens functions for multilayered spheroidal structures. i formulation. *Transactions on Microwave Theory and Techniques*, 49(3):532–541.

[Liu et al., 2007] Liu, S., Zeng, Z., and Deng, L. (2007). FDTD simulations for ground penetrating radar in urban applications. *Journal of Geophysics and Engineering*, 4(3):262–267.

[Luebbers et al., 1993] Luebbers, R., Steich, D., and Kunz, K. (1993). FDTD calculation of scattering from frequency-dependent materials. *IEEE Transactions on Antennas and Propagation*, 41(9):1249–1257.

[Maier, 2007] Maier, S. A. (2007). *Plasmonics: Fundamental and Applications*. Springer.

[Makinen et al., 2002] Makinen, R., Juntunen, J., and Kivikoski, M. (2002). An improved thin-wire model for FDTD. *IEEE Transactions on Microwave Theory and Techniques*, 50(5):1245–1255.

[Maradudin A., 2014] Maradudin A., J. R. Sambles, W. L. B. (2014). *Modern Plasmonics*, volume 4. Elsevier Science.

[Mei K. K., 1992] Mei K. K., F. J. (1992). Superabsorption-a method to improve absorbing boundary conditions (electromagnetic waves). *IEEE Transactions on Antennas and Propagation*, 40(9):1001–1010.

[Milton, 2003] Milton, K. A. (2003). The casimir effect: Physical manifestations of zero-point energy the casimir effect: Physical manifestations of zero-point energy , k. a. milton world scientific, river edge, n.j., 2001. $87.00 (301 pp.). ISBN 981-02-4397-9. *Physics Today*, 56(1):49–50.

[Mur, 1981] Mur, G. (1981). Absorbing boundary conditions for the finite-difference approximation of the time-domain electromagnetic-field equations. *IEEE Transactions on Electromagnetic Compatibility*, EMC-23(4):377–382.

[Narayanaswamy A., 2010] Narayanaswamy A., C. G. (2010). Dyadic greens functions and electromagnetic local density of states. *Journal of Quantitative Spectroscopy and Radiative Transfer*, 111(12-13):1877–1884.

[Nguyen et al., 2015] Nguyen, A. H., Lee, J., Choi, H. I., Kwak, H. S., and Sim, S. J. (2015). Fabrication of plasmon length-based surface enhanced raman scattering for multiplex detection on microfluidic device. *Biosensors and Bioelectronics*, 70:358–365.

[Novotny L., 2009] Novotny L., H. B. (2009). *Principles of Nano-Optics*. Cambridge University Press.

[Okoniewski M., 2006] Okoniewski M., O. E. (2006). Drude dispersion in ADE FDTD revisited. *Electronics Letters*, 42(9):503.

[Paul S. R., 2016] Paul S. R., M. S. K. (2016). Importance of FDTD in plasmonic devices. In *2016 IEEE Students Conference on Electrical, Electronics and Computer Science (SCEECS)*. IEEE.

[Paulus et al., 2000] Paulus, M., Gay-Balmaz, P., and Martin, O. J. F. (2000). Accurate and efficient computation of the green's tensor for stratified media. *Physical Review E*, 62(4):5797–5807.

[Pelton, 2015] Pelton, M. (2015). Modified spontaneous emission in nanophotonic structures. *Nature Photonics*, 9(7):427–435.

[Perez-Ocon et al., 2006] Perez-Ocon, F., Pozo, A., Jimenez, J., and Hita, E. (2006). Fast single-mode characterization of optical fiber by finite-difference time-domain method. *Journal of Lightwave Technology*, 24(8):3129–3136.

[Pontalti et al., 2002] Pontalti, R., Nadobny, J., Wust, P., Vaccari, A., and Sullivan, D. (2002). Investigation of static and quasi-static fields inherent to the pulsed FDTD method. *IEEE Transactions on Microwave Theory and Techniques*, 50(8):2022–2025.

[Purcell, 1995] Purcell, E. M. (1995). Spontaneous emission probabilities at radio frequencies. In *Confined Electrons and Photons*, pages 839–839. Springer US.

[Rahmat-Samii Y., 2006] Rahmat-Samii Y., J. K. (2006). Implanted antennas in medical wireless communications. *Synthesis Lectures on Antennas*, 1(1):1–82.

[Reddy V. S., 1999] Reddy V. S., R. G. (1999). Finite difference time domain fdtd analysis of microwave circuits a review with examples. *IETE Journal of Research*, 45(1):3–20.

[Roden J. A., 2000] Roden J. A., G. S. D. (2000). Convolution PML (CPML): An efficient FDTD implementation of the CFS-PML for arbitrary media. *Microwave and Optical Technology Letters*, 27(5):334–339.

[Ru E. C., 2012] Ru E. C., E. P. (2012). Single-molecule surface-enhanced raman spectroscopy. *Annual Review of Physical Chemistry*, 63(1):65–87.

[Ru E. C., 2009] Ru E. C., E. P. G. (2009). *Principles of Surface-Enhanced Raman Spectroscopy*. Elsevier.

[Scheel S., 2008] Scheel S., B. S. (2008). Macroscopic quantum electrodynamics - concepts and applications. *Acta Physica Slovaca. Reviews and Tutorials*, 58(5).

[Schneider, 2012] Schneider, J. B. (2012). *Understanding the Finite-Difference Time-Domain Method*.

[Sepulveda, 2017] Sepulveda, J. (2017). Estudio computacional de plasmones localizados en nanoparticulas de plata.

[Sullivan, 1992] Sullivan, D. (1992). Frequency-dependent FDTD methods using z transforms. *IEEE Transactions on Antennas and Propagation*, 40(10):1223–1230.

[Taflove A., 2005] Taflove A., S. C. H. (2005). *Computational Electrodynamics: The Finite-Difference Time-Domain Method.* ARTECH HOUSE, INC., 3 edition.

[Taflove A., 2013] Taflove A., Ardavan Oskooi, S. G. J. (2013). *Computational Electrodynamics, Photonics and Nanotechnology*. Artech House.

[Takayama Y., 2002] Takayama Y., K. W. (2002). Reinterpretation of the auxiliary differential equation method for FDTD. *IEEE Microwave and Wireless Components Letters*, 12(3):102–104.

[Teixeira, 2008] Teixeira, F. L. (2008). Time-domain finite-difference and finite-element methods for maxwell equations in complex media. *IEEE Transactions on Antennas and Propagation*, 56(8):2150–2166.

[Tirkas P. A., 1992] Tirkas P. A., B. C. A. (1992). Finite-difference time-domain method for antenna radiation. *IEEE Transactions on Antennas and Propagation*, 40(3):334–340.

[Ueno K., 2013] Ueno K., M. H. (2013). Surface plasmon-enhanced photochemical reactions. *Journal of Photochemistry and Photobiology C: Photochemistry Reviews*, 15:31–52.

[Valev et al., 2013] Valev, V. K., Baumberg, J. J., Sibilia, C., and Verbiest, T. (2013). Chirality and chiroptical effects in plasmonic nanostructures: Fundamentals, recent progress, and outlook. *Advanced Materials*, 25(18):2517–2534.

[Vlack, 2012] Vlack, C. V. (2012). Dyadic green functions and their applications in classical and quantum nanophotonics.

[Vogel W., 2006] Vogel W., W. D. G. (2006). *Quantum Optics*. Wiley-VCH, 3 edition.

[Vuckovic et al., 2000] Vuckovic, J., Painter, O. J., Xu, Y., Yariv, A., and Scherer, A. (2000). Fdtd calculation of the spontaneous emission coupling factor in optical microcavities. In Perry, J. W. and Scherer, A., editors, *Micro- and Nano-photonic Materials and Devices*. SPIE.

[Wang et al., 2019] Wang, S., Scholes, G. D., and Hsu, L.-Y. (2019). Quantum dynamics of a molecular emitter strongly coupled with surface plasmon polaritons: A macroscopic quantum electrodynamics approach. *The Journal of Chemical Physics*, 151(1):014105.

[Willets K. A., 2007] Willets K. A., V. D. R. P. (2007). Localized surface plasmon resonance spectroscopy and sensing. *Annual Review of Physical Chemistry*, 58(1):267–297.

[Wu et al., 2018] Wu, J.-S., Lin, Y.-C., Sheu, Y.-L., and Hsu, L.-Y. (2018). Characteristic distance of resonance energy transfer coupled with surface plasmon polaritons. *The Journal of Physical Chemistry Letters*, 9(24):7032–7039.

[Xu, 2014] Xu, Y. (2014). Performance analysis of point source model with coincident phase centers in fdtd. Master's thesis.

[Yang et al., 2015] Yang, H. U., D'Archangel, J., Sundheimer, M. L., Tucker, E., Boreman, G. D., and Raschke, M. B. (2015). Optical dielectric function of silver. *Physical Review B*, 91(23).

[Yee, 1966] Yee, K. (1966). Numerical solution of initial boundary value problems involving maxwell's equations in isotropic media. *IEEE Transactions on Antennas and Propagation*, 14(3):302–307.

[Yokoyama M., 2005] Yokoyama M., N. S. (2005). Finite-difference time-domain simulation of two-dimensional photonic crystal surface-emitting laser. *Optics Express*, 13(8):2869.

Appendix A

Green's Function

The Green's function is the solution of a wave equation for a point source

$$\left(\nabla^2 + k^2\right) \psi\left(r\right) = s\left(\mathbf{r}\right). \tag{A.0.1}$$

We seek the Green's function in the same volume V, which is the solution to the following equation

$$\left(\nabla^2 + k^2\right) g\left(\mathbf{r}, \mathbf{r}'\right) = -\delta\left(r - r'\right). \tag{A.0.2}$$

Given $g\left(\mathbf{r}, \mathbf{r}'\right)$, is possible to find $\psi\left(\mathbf{r}\right)$, from the principle of linear superposition, since $g\left(\mathbf{r}, \mathbf{r}'\right)$ is the solution of the equation (A.0.1) due to a point source on the right-hand side. The solution of a arbitrary source is

$$\psi\left(\mathbf{r}\right) = \int_{V'} dV' g\left(\mathbf{r}, \mathbf{r}'\right) s\left(\mathbf{r}'\right) \tag{A.0.3}$$

which is a linear superposition in a volume V' of the equation (A.0.1).

To find the solution of equation (A.0.2), solving with $\mathbf{r}' = 0$ at the origin

$$\left(\nabla^2 + k^2\right) g\left(\mathbf{r}\right) = -\delta\left(x\right)\delta\left(y\right)\delta\left(z\right) \tag{A.0.4}$$

then for $r \neq 0$, the homogeneous spherically symmetric solution is given by

$$g\left(r\right) = C\frac{e^{ikr}}{r} + D\frac{e^{-ikr}}{r} \tag{A.0.5}$$

since there are not source at the infinity, this imply that only out going solution can exist, hence

$$g\left(r\right) = C\frac{e^{ikr}}{r}. \tag{A.0.6}$$

The constant C is found by matching the singularities at the origin on both sides, substitute the equation (A.0.6) into (A.0.2) and integrate the equation (A.0.2) over a small volume about the origin to yield

$$\int_{\Delta V} dV \boldsymbol{\nabla} \cdot \boldsymbol{\nabla} \frac{Ce^{ikr}}{r} + \int_{\Delta V} dV k^2 \frac{Ce^{ikr}}{r} = -1 \tag{A.0.7}$$

the second integral vanishes when $\Delta V \to 0$, because $dV = 4\pi r^2 dr$. Using Gauss's theorem in the first integral we obtain

$$\lim_{r\to 0} 4\pi r^2 \frac{d}{dr} C \frac{e^{ikr}}{r} = -1 \tag{A.0.8}$$

then $C = \frac{1}{4\pi}$. Finally the solution of (A.0.1) is

$$\psi(r) = \int_V dr' \frac{e^{ik|\mathbf{r}-\mathbf{r}'|}}{4\pi|\mathbf{r}-\mathbf{r}'|} s(r') . \tag{A.0.9}$$

Appendix B

Integral relation of the Green's tensor

For a given absorbing and dispersing body with $\mathrm{Im}\left[\epsilon\left(\mathbf{r},\omega\right)\right]>0,\ \mathrm{Im}\left[\mu\left(\mathbf{r},\omega\right)\right]>0$ the classical Green's tensor is defined by the Helmholtz equation

$$\left[\boldsymbol{\nabla}\times\frac{1}{\mu\left(\mathbf{r},\omega\right)}\boldsymbol{\nabla}\times-k_0^2\epsilon\left(\mathbf{r},\omega\right)\right]\overleftrightarrow{\mathbf{G}}\left(\mathbf{r},\mathbf{r}';\omega\right)=\boldsymbol{\delta}\left(\mathbf{r}-\mathbf{r}'\right). \tag{B.0.1}$$

The permittivity and permeability appearing in the defining equation of Green's tensor are causal response functions and hence analytic functions of frequency in the upper half of the complex ω plane including the real axis, apart from a simple pole at $\omega=0$ occurring in the permittivity of metals. The validity of the Schwarz reflection principle $\epsilon^*\left(\mathbf{r},\omega\right)=\epsilon\left(\mathbf{r},-\omega^*\right),\ \mu^*\left(\mathbf{r},\omega\right)=\mu\left(\mathbf{r},-\omega^*\right)$, then

$$\overleftrightarrow{\mathbf{G}}^*\left(\mathbf{r},\mathbf{r}';\omega\right)=\overleftrightarrow{\mathbf{G}}\left(\mathbf{r},\mathbf{r}';-\omega^*\right) \tag{B.0.2}$$

the inverse of the Helmholtz operator must be

$$\overleftrightarrow{\mathbf{G}}\left(\mathbf{r},\mathbf{r}';\omega\right)\left[\times\overleftarrow{\boldsymbol{\nabla}}'\times\frac{1}{\mu\left(\mathbf{r}',\omega\right)}\overleftarrow{\boldsymbol{\nabla}}'-k_0^2\epsilon\left(\mathbf{r}',\omega\right)\right]=\boldsymbol{\delta}\left(\mathbf{r}-\mathbf{r}'\right). \tag{B.0.3}$$

after exchanging $\mathbf{r}$ and $\mathbf{r}'$, this equation can be written as

$$\left[\boldsymbol{\nabla}\times\frac{1}{\mu\left(\mathbf{r},\omega\right)}\boldsymbol{\nabla}\times-k_0^2\epsilon\left(\mathbf{r},\omega\right)\right]\overleftrightarrow{\mathbf{G}}^{\mathrm{T}}\left(\mathbf{r},\mathbf{r}';\omega\right)=\boldsymbol{\delta}\left(\mathbf{r}-\mathbf{r}'\right) \tag{B.0.4}$$

using the Onsanger reciprocity

$$\overleftrightarrow{\mathbf{G}}^{\mathrm{T}}\left(\mathbf{r},\mathbf{r}';\omega\right)=\overleftrightarrow{\mathbf{G}}\left(\mathbf{r}',\mathbf{r};\omega\right). \tag{B.0.5}$$

The Green's tensor can also be used to derive a useful integral equation, multiplying (B.0.1) for $\overleftrightarrow{\mathbf{G}}\left(\mathbf{s},\mathbf{r}';\omega\right)$ with $\overleftrightarrow{\mathbf{G}}^*\left(\mathbf{r},\mathbf{s};\omega\right)$ from the left and integrating over s, we obtain

$$-\int d^3s\left[\overleftrightarrow{\mathbf{G}}^*\left(\mathbf{r},\mathbf{s};\omega\right)\times\overleftarrow{\boldsymbol{\nabla}}_s\cdot\frac{1}{\mu\left(\mathbf{s},\omega\right)}\boldsymbol{\nabla}_s\times\overleftrightarrow{\mathbf{G}}\left(\mathbf{s},\mathbf{r}';\omega\right)\right. \tag{B.0.6}$$

$$+k_0^2\epsilon\left(\mathbf{s},\omega\right)\overleftrightarrow{\mathbf{G}}^*\left(\mathbf{r},\mathbf{s};\omega\right)\cdot\overleftrightarrow{\mathbf{G}}\left(\mathbf{s},\mathbf{r}';\omega\right)\Big]=\overleftrightarrow{\mathbf{G}}^*\left(\mathbf{r},\mathbf{r}';\omega\right).$$

Similarly, taken the complex conjugate of (B.0.3) for $\overleftrightarrow{\mathbf{G}}\left(\mathbf{r},\mathbf{s};\omega\right)$, multiplying the result with $\overleftrightarrow{\mathbf{G}}\left(\mathbf{s},\mathbf{r}';\omega\right)$ and integrating over s one obtains

$$-\int d^3s\left[\overleftrightarrow{\mathbf{G}}^*\left(\mathbf{r},\mathbf{s};\omega\right)\times\overleftarrow{\boldsymbol{\nabla}}_s\cdot\frac{1}{\mu^*\left(\mathbf{s},\omega\right)}\boldsymbol{\nabla}_s\times\overleftrightarrow{\mathbf{G}}\left(\mathbf{s},\mathbf{r}';\omega\right)\right. \tag{B.0.7}$$

$$\left.+k_0^2\epsilon^*\left(\mathbf{s},\omega\right)\overleftrightarrow{\mathbf{G}}^*\left(\mathbf{r},\mathbf{s};\omega\right)\cdot\overleftrightarrow{\mathbf{G}}\left(\mathbf{s},\mathbf{r}';\omega\right)\right]=\overleftrightarrow{\mathbf{G}}\left(\mathbf{r},\mathbf{r}';\omega\right).$$

Subtracting these equations and using $\mathrm{Im}\left[\mathrm{z}\right]=\left(z-z^*\right)/2\mathrm{i}$ and taking the complex conjugate again, we find the integral relation

$$\int d^3s\left\{-\frac{\mathrm{Im}\left[\mu\left(\mathbf{s},\omega\right)\right]}{\left|\mu\left(\mathbf{s},\omega\right)\right|^2}\left[\overleftrightarrow{G}\left(\mathbf{r},\mathbf{s},\omega\right)\times\overleftarrow{\boldsymbol{\nabla}}\right]\cdot\left[\boldsymbol{\nabla}_s\times\overleftrightarrow{\mathbf{G}}^*\left(\mathbf{s},\mathbf{r}',\omega\right)\right]\right. \tag{B.0.8}$$

$$\left.+k_0^2\mathrm{Im}\left[\epsilon\left(\mathbf{s},\omega\right)\right]\overleftrightarrow{\mathbf{G}}\left(\mathbf{r},\mathbf{s},\omega\right)\cdot\overleftrightarrow{\mathbf{G}}^*\left(\mathbf{s},\mathbf{r}',\omega\right)\right\}=\mathrm{Im}\left[\overleftrightarrow{\mathbf{G}}\left(\mathbf{r},\mathbf{r}',\omega\right)\right]$$

Appendix C

Commutation relation

According to the definition of the commutator

$$\left[\hat{a}\left(\mathbf{r},\omega\right),\hat{a}^{\dagger}\left(\mathbf{r}',\omega'\right)\right]=\hat{a}\left(\mathbf{r},\omega\right)\hat{a}^{\dagger}\left(\mathbf{r}',\omega'\right)-\hat{a}^{\dagger}\left(\mathbf{r}',\omega'\right)\hat{a}\left(\mathbf{r},\omega\right) \tag{C.0.1}$$

and using the equation (3.2.7) we obtain

$$\left[\hat{a}\left(\mathbf{r},\omega\right),\hat{a}^{\dagger}\left(\mathbf{r}',\omega'\right)\right]=\frac{1}{\hbar^{2}g\left(\mathbf{r},\omega\right)g\left(\mathbf{r}',\omega'\right)}\sum_{\lambda\lambda'}\int d^{3}s\int d^{3}s'\left[\mathbf{d}^{10}\cdot\overleftrightarrow{\mathbf{G}}_{\lambda}\left(\mathbf{r},\mathbf{s},\omega\right)\cdot\hat{\mathbf{f}}\left(\mathbf{s},\omega\right)\right.$$

$$\left.\mathbf{d}^{01}\cdot\overleftrightarrow{\mathbf{G}}_{\lambda'}^{*\mathrm{T}}\left(\mathbf{r}',\mathbf{s}',\omega'\right)\cdot\hat{\mathbf{f}}^{\dagger}\left(\mathbf{s}',\omega'\right)-\mathbf{d}^{01}\cdot\overleftrightarrow{\mathbf{G}}_{\lambda'}^{*\mathrm{T}}\left(\mathbf{r}',\mathbf{s}',\omega'\right)\cdot\hat{\mathbf{f}}^{\dagger}\left(\mathbf{s}',\omega'\right)\mathbf{d}^{10}\cdot\overleftrightarrow{\mathbf{G}}_{\lambda}\left(\mathbf{r},\mathbf{s},\omega\right)\cdot\hat{\mathbf{f}}\left(\mathbf{s},\omega\right)\right] \tag{C.0.2}$$

to simplify the notation, we use Einstein summation notation

$$\left[\hat{a}\left(\mathbf{r},\omega\right),\hat{a}^{\dagger}\left(\mathbf{r}',\omega'\right)\right]=\frac{1}{\hbar^{2}g\left(\mathbf{r},\omega\right)g\left(\mathbf{r}',\omega'\right)}\sum_{\lambda\lambda'}\int d^{3}s\int d^{3}s'$$

$$\times\left[\hat{f}_{\lambda}^{j}\left(\mathbf{s},\omega\right)\hat{f}_{\lambda'}^{i'\dagger}\left(\mathbf{s}',\omega'\right)-\hat{f}_{\lambda'}^{i'\dagger}\left(\mathbf{s}',\omega'\right)\hat{f}_{\lambda}^{j}\left(\mathbf{s},\omega\right)\right]d_{i}^{10}G_{ij}\left(\mathbf{r},\mathbf{s},\omega\right)d_{j'}^{01}G_{i'j'}^{*\mathrm{T}}\left(\mathbf{r}',\mathbf{s}',\omega'\right) \tag{C.0.3}$$

and using the equations (5) yields

$$\left[\hat{a}\left(\mathbf{r},\omega\right),\hat{a}^{\dagger}\left(\mathbf{r}',\omega'\right)\right]=\frac{1}{\hbar^{2}g\left(\mathbf{r},\omega\right)g\left(\mathbf{r}',\omega\right)}\sum_{\lambda\lambda'}\int d^{3}s\int d^{3}s'$$

$$d_{i}^{10}G_{ij}\left(\mathbf{r},\mathbf{s},\omega\right)d_{j'}^{01}G_{i'j'}^{*\mathrm{T}}\left(\mathbf{r}',\mathbf{s}',\omega\right)\delta_{i'j}\delta_{\lambda\lambda'}\delta\left(\mathbf{s}-\mathbf{s}'\right)\delta\left(\omega-\omega'\right) \tag{C.0.4}$$

using the delta functions

$$\left[\hat{a}\left(\mathbf{r},\omega\right),\hat{a}^{\dagger}\left(\mathbf{r}',\omega'\right)\right]=\frac{1}{\hbar^{2}g\left(\mathbf{r},\omega\right)g\left(\mathbf{r}',\omega\right)}\sum_{\lambda}\int d^{3}s$$

$$d_{i}^{10}G_{ij}\left(\mathbf{r},\mathbf{s},\omega\right)G_{jj'}^{*\mathrm{T}}\left(\mathbf{r}',\mathbf{s}',\omega\right)\delta\left(\omega-\omega'\right)d_{j'}^{01} \tag{C.0.5}$$

finally using the integral relation (3.1.18) we obtain

$$\left[\hat{a}\left(\mathbf{r},\omega\right),\hat{a}^{\dagger}\left(\mathbf{r}',\omega'\right)\right]=$$

$$\frac{1}{\hbar^{2}g\left(\mathbf{r},\omega\right)g\left(\mathbf{r}',\omega\right)}\mathbf{d}^{10}\cdot\mathrm{Im}\left[\overleftrightarrow{\mathbf{G}}\left(\mathbf{r},\mathbf{r}',\omega\right)\right]\cdot\mathbf{d}^{01}\frac{\hbar\mu_{0}}{\pi}\omega^{2}\delta\left(\omega-\omega'\right) \tag{C.0.6}$$

Appendix D

Derivation of the dynamic equations

From the Schrodinger equation, we have

$$i\hbar\frac{\partial}{\partial t}\left|\psi\left(t\right)\right\rangle = \hat{H}_{tot}\left|\psi\left(t\right)\right\rangle \tag{D.0.1}$$

using the ansatz, equation (3.3.1), the left hand side turns be

$$i\hbar\frac{\partial}{\partial t}\left|\psi\left(t\right)\right\rangle = i\hbar\left[\left(\dot{C}_{1\{0\}}\left(t\right) - i\omega_{10}C_{1\{0\}}\left(t\right)\right)e^{-i\omega_{10}t}\left|1\right\rangle\left|\{0\}\right\rangle\right. \tag{D.0.2}$$

$$\left. + \int_0^\infty d\omega\left(\dot{C}_{0\{1\}}\left(\mathbf{r}_A,\omega,t\right) - i\omega C_{0\{1\}}\left(\mathbf{r}_A,\omega,t\right)\right)e^{-i\omega t}\left|0\right\rangle\left|\{\mathbf{1}\left(\mathbf{r}_A,\omega\right)\}\right\rangle\right].$$

For the right hand side, we can separate the total Hamiltonian equation (3.2.1) and evaluated as follow

$$\hat{H}_A\left|\psi\left(t\right)\right\rangle = \hbar\omega_{10}C_{1\{0\}}\left(t\right)e^{-i\omega_{10}t}\left|1\right\rangle\left|\{0\}\right\rangle \tag{D.0.3a}$$

$$\hat{H}_F\left|\psi\left(t\right)\right\rangle = \int_0^\infty d\omega\hbar\omega C_{0\{1\}}\left(\mathbf{r}_A,\omega,t\right)e^{-i\omega t}\left|0\right\rangle\left|\{\mathbf{1}\left(\mathbf{r}_A,\omega\right)\}\right\rangle \tag{D.0.3b}$$

$$\hat{H}_{AF}\left|\psi\left(t\right)\right\rangle = \int_0^\infty d\omega\hbar g\left(\mathbf{r}_A,\omega\right)C_{0\{1\}}\left(\mathbf{r}_A,\omega,t\right)e^{-i\omega t}\left|1\right\rangle\left|\{0\}\right\rangle \tag{D.0.3c}$$

$$+ \int_0^\infty d\omega\hbar g\left(\mathbf{r}_A,\omega\right)C_{1\{0\}}\left(t\right)e^{-i\omega_{10}t}\left|0\right\rangle\left|\{\mathbf{1}\left(\mathbf{r}_A,\omega\right)\}\right\rangle$$

multiplying the Schrodinger equation by $\langle 1|\langle\{0\}|$, we obtain

$$i\hbar\dot{C}_{1\{0\}}\left(t\right)e^{-i\omega_{10}t} = \int_0^\infty d\omega\hbar g\left(\mathbf{r}_A,\omega\right)C_{0\{1\}}\left(\mathbf{r}_A,\omega,t\right)e^{-i\omega t} \tag{D.0.4}$$

and multiplying by $\langle 0| \langle \{\mathbf{1}(\mathbf{r}_A, \omega)\}|$, we obtain

$$i\hbar \dot{C}_{0\{1\}}(\mathbf{r}_A, \omega, t) e^{-i\omega t} = \hbar g(\mathbf{r}_A, \omega) C_{1\{0\}}(t) e^{-i\omega_{10} t} \tag{D.0.5}$$

we can formally integrate the equation (D.0.5) with $C_{0\{1\}}(\mathbf{r}_A, \omega, t = 0) = C_{0\{1\}}(\mathbf{r}_A, \omega, 0)$, and we obtain

$$C_{0\{1\}}(\mathbf{r}_A, \omega, t) = -\int_0^t dt' ig(\mathbf{r}_A, \omega) e^{it'(\omega - \omega_{10})} C_{1\{0\}}(t') + C_{0\{1\}}(\mathbf{r}_A, \omega, 0) \tag{D.0.6}$$

then we replace the equation (D.0.6) into (D.0.4)

$$\dot{C}_{1\{0\}}(t) = -\int_0^t dt' \int_0^\infty d\omega g^2(\mathbf{r}_A, \omega) e^{-i\left(t - t'\right)(\omega - \omega_{10})} C_{1\{0\}}(t') \tag{D.0.7}$$

$$- i \int_0^\infty d\omega g(\mathbf{r}_A, \omega) e^{-i(\omega - \omega_{10})t} C_{0\{1\}}(\mathbf{r}_A, \omega, 0)$$

using the equation (3.2.8), we obtain the equation (3.3.3).

Using the same process for the electronic coefficient we obtain

$$\dot{C}_{0\{1\}}(\mathbf{r}_A, \omega, t) = -ig(\mathbf{r}_A, \omega) e^{i(\omega - \omega_{10})t} C_{1\{0\}}(0) \tag{D.0.8}$$

$$- g(\mathbf{r}_A, \omega) e^{i(\omega - \omega_{10})t} \int_0^t dt' \int_0^\infty d\omega g(\mathbf{r}_A, \omega) e^{-i(\omega - \omega_{10})t'} C_{0\{1\}}(\mathbf{r}_A, \omega, t').$$